Renewable Energy 112 (2017) 280–301

Contents lists available at ScienceDirect

Renewable Energy

journal homepage: www.elsevier.com/locate/renene

Establishing a fully coupled CFD analysis tool for floating offshore wind turbines

Yuanchuan Liu [a], Qing Xiao [a, *], Atilla Incecik [a], Christophe Peyrard [b], Decheng Wan [c]

[a] Department of Naval Architecture, Ocean and Marine Engineering, University of Strathclyde, Glasgow G4 0LZ, UK
[b] Saint-Venant Hydraulics Laboratory (Électricité de France, ENPC, Cerema), Université Paris-Est, 6 quai Watier, 78400 Chatou, France
[c] State Key Laboratory of Ocean Engineering, School of Naval Architecture, Ocean and Civil Engineering, Shanghai Jiao Tong University, Collaborative Innovation Center for Advanced Ship and Deep-Sea Exploration, Shanghai 200240, China

ARTICLE INFO

Article history:
Received 30 June 2016
Received in revised form
6 March 2017
Accepted 25 April 2017
Available online 28 April 2017

Keywords:
Floating offshore wind turbine
Computational fluid dynamics
Fluid-structure interaction
OpenFOAM
Sliding mesh technique

ABSTRACT

An accurate study of a floating offshore wind turbine (FOWT) system requires interdisciplinary knowledge about wind turbine aerodynamics, floating platform hydrodynamics and mooring line dynamics, as well as interaction between these discipline areas. Computational Fluid Dynamics (CFD) provides a new means of analysing a fully coupled fluid-structure interaction (FSI) system in a detailed manner. In this paper, a numerical tool based on the open source CFD toolbox OpenFOAM for application to FOWTs will be described. Various benchmark cases are first modelled to demonstrate the capability of the tool. The OC4 DeepCWind semi-submersible FOWT model is then investigated under different operating conditions.

With this tool, the effects of the dynamic motions of the floating platform on the wind turbine aerodynamic performance and the impact of the wind turbine aerodynamics on the behaviour of the floating platform and on the mooring system responses are examined. The present results provide quantitative information of three-dimensional FSI that may complement related experimental studies. In addition, CFD modelling enables the detailed quantitative analysis of the wind turbine flow field, the pressure distribution along blades and their effects on the wind turbine aerodynamics and the hydrodynamics of the floating structure, which is difficult to carry out experimentally.

1. Introduction

The harnessing of wind energy as a clean and renewable energy source has undergone rapid growth over the last decade. According to a report published by the European Wind Energy Association [10], in 2014, 11,791 MW of wind power capacity, which is more than gas and coal combined, was installed in the EU. By the end of 2014, the cumulative wind power capacity has reached 128.8 GW and can meet the demand of 10.2% of Europe's electricity, which is a remarkable increase from 2.4% in 2000. It is also expected that wind energy will account for at least 43–45% of all renewable energy by 2030. In the past few years, an increasing number of wind turbines are installed in offshore areas mainly due to the higher mean wind speed offshore than onshore. In 2015, the total cumulative offshore wind installations has exceeded 10 GW [10]. Along with the success of the emerging offshore wind industry, a new generation of floating offshore wind turbines (FOWTs) is under development. Following the success of the world's first full scale 2.3 MW FOWT demonstration project Hywind near the coast of Norway [46,51], the Scottish government granted the Norwegian energy company, Statoil, a license for the world's largest floating wind farm consisting of five 6 MW floating turbines operating in waters exceeding 100 m of depth in the North Sea off the coast of Peterhead, Scotland [4].

Installing floating wind turbines in deep water has many advantages [19]. For instance, there are vast deep-water sites suitable for the installation of floating offshore wind turbines while fixed wind turbines can only be installed in the areas with shallow water depth. In addition, wind resource is even more abundant in offshore areas far off the coast than in near-shore waters and the public concerns on visual and environmental impacts, caused by onshore and near-shore turbines, would be minimised.

However, from the perspective of engineering design and operation, floating offshore wind turbines have several important

* Corresponding author.
E-mail address: qing.xiao@strath.ac.uk (Q. Xiao).

http://dx.doi.org/10.1016/j.renene.2017.04.052

Nomenclature

α	Volume Fraction Variable for Two-phase Fluid Flow
μ_{eff}	Effective Dynamic Viscosity of Fluid
ν	Fluid Kinematic Viscosity
ν_t	Eddy Kinematic Viscosity
ρ	Fluid Density
C_p	Pressure Coefficient
p	Fluid Flow Pressure
r	Distance from Blade Section to Rotor Centre
R	Rotor Blade Radius
AMI	Arbitrary Mesh Interface
BEM	Blade Element Momentum
CFD	Computational Fluid Dynamics
DCI	Domain Connectivity Information
DoF	Degrees of Freedom
EWEA	European Wind Energy Association
FAST	Fatigue, Aerodynamics, Structures, and Turbulence
FOWT	Floating Offshore Wind Turbine
GDW	Generalized Dynamic Wake
MARIN	Maritime Research Institute Netherlands
NREL	National Renewable Energy Laboratory
OC3	Offshore Code Comparison Collaboration
OC4	Offshore Code Comparison Collaboration Continuation
RAO	Response Amplitude Operator
SST	Shear Stress Transport
TLP	Tension Leg Platform
UBEM	Unsteady Blade Element Momentum
UDF	User Defined Function
VOF	Volume of Fluid

challenges, which need to be overcome before FOWTs could be widely applied. One of the common challenges in relation to the device sustainability is the accurate prediction of FOWT's time-dependent power output, system dynamic responses and structural loadings under variable wind and wave conditions. A floating offshore wind turbine is a rather complex system consisting of a wind turbine, a floating platform supporting the turbine and a mooring system to maintain the position of the system. The wind turbine and its supporting platform are coupled in the way that the aerodynamic force acting on the turbine contributes to the overall system loading, thus influences the dynamic response of the floating platform. Meanwhile the six degree-of-freedom platform motion affects the position/orientation of the turbine, which modifies the relative wind velocity experienced by the turbine and thus its aerodynamic performance. The inclusion of the mooring system further complicates the overall FOWT system analysis.

In recent years, a number of experimental tests have been carried out to study the dynamic responses of different FOWT designs under various environmental conditions [8,9,22,45]. However, it is well known that model tests are rather expensive. In addition, as Froude scaling is usually adopted in the experiments where Reynolds similarity law is hard to achieve at the same time, inaccuracy is introduced when the model test results are applied to the full-scale devices. As a result, many researchers have been developing numerical modelling tools for full-scale FOWT analysis. Among the most well-known tools developed is the software package named FAST (Fatigue, Aerodynamics, Structures, and Turbulence), developed by the National Renewable Energy Laboratory (NREL). As it is claimed and used by various researchers, FAST is able to perform fully coupled time-domain aero-hydro-servo-elastic simulations for FOWT systems [3,8,20].

In principle, FAST uses an input of a hydrodynamic database computed by an external potential-flow solver (such as WAMIT) to predict hydrodynamic loading. As potential-based methods inherently cannot take viscous effects into consideration, a quadratic damping model from Morison's equation is normally adopted to include the drag force [8,48], which requires an additional quadratic damping coefficient relying on experimental test data. In addition, the damping model is unable to consider transverse or lift forces associated with vortex shedding [5], which significantly affects the accuracy of the predicted motion responses of a system in transverse directions. In terms of wind turbine aerodynamic loading, FAST adopts a conventional Blade Element Momentum (BEM) method with various empirical and semi-empirical correction models. As the wind flow conditions are rather complex for an FOWT, considering the dynamic interaction between the wind turbine and its wake due to the platform motions, the BEM method may not be well valid [40,50].

Apart from the BEM methods, vortex methods are also used to model wind turbine aerodynamics. With the use of lifting lines or surfaces to represent rotor blades, trailing and shed wake in vortex methods, one is able to describe the 3D flow around a wind turbine and to have a better insight into the flow development than with the use of the BEM methods [18,40]. However, as they are based on the assumption of inviscid flow condition, the viscous effects are neglected with the application of potential flow models, which may cause significant problems when strong flow separation occurs around turbine blades. In addition, vortex methods also tend to suffer from the stability problems when vortex elements approach each other as indicated by Hansen et al. [14].

In contrast to the aforementioned methods, as Computational Fluid Dynamics (CFD) methods inherently takes fluid viscosity into account, the hydrodynamic drag forces acting on a floating platform can be directly calculated in both inline and transverse directions. Furthermore, CFD methods are able to model the dynamic interaction between fluid flow, wind turbine and floating platform. With the use of a CFD tool, direct modelling of FOWT systems is possible and full-scale simulations can be performed. Therefore, the scale effects will no longer be present in the predictions. With these advantages, there is an increasing trend to analyse FOWT systems using CFD tools.

As mentioned earlier, a fully coupled aero-hydro study of FOWT includes (a) the investigation of wind turbine aerodynamics; (b) the investigation of floating platform hydrodynamics and mooring line dynamics; and (c) the coupling between the wind turbine and the floating platform. To ease the complexity of the system, most of the existing investigations of FOWTs either simplify the aerodynamics of wind turbines or focus on aerodynamic loading by restricting the motions of floating platforms in a prescribed manner.

Within the group of work studying the hydrodynamic loading and motion response of a floating support structure of an FOWT while simplifying the wind turbine aerodynamic loading, typical papers include Nematbakhsh et al. [30,31] and Tran and Kim [48]. Nematbakhsh et al. [31] developed a CFD model based on an immersed boundary method and studied the motion of a 5 MW spar buoy type FOWT in moderate and extreme sea states under irregular wave conditions. With their method, they successfully captured strong nonlinear effects, such as the complete submergence of the platform tank and tether slacking, which is rather difficult to accurately predict with commonly used simplified

models like the ones used in FAST. In a subsequent work, Nematbakhsh et al. [30] extended their study for wave-induced responses of a Tension Leg Platform (TLP) wind turbine in deep water. A comparison between the results from the CFD model and a finite element model based on the potential flow theory indicated that large discrepancies exist between the results obtained from these two different methods when the wave amplitude is large. Tran and Kim [48] investigated the hydrodynamic responses of the DeepC-Wind semi-submersible platform using the commercial CFD software package STAR-CCM+. Their modelling results showed generally good agreement with experimental test data. Using an in-house CFD solver (naoe-FOAM-SJTU), Zhao and Wan [53] studied the effects of the presence of a wind turbine on a semi-submersible floating platform in waves. However, the influence of the wind turbine on the platform was simplified as an equivalent force without the inclusion of a fully resolved turbine model. Nonetheless, the effect of the wind turbine on the floating platform was apparently observed, especially for the platform pitch motion associated with a high wind speed.

A full CFD analysis of wind turbine aerodynamics while constraining the motion of a floating platform was carried out by Tran et al. [47]. Instead of modelling a floating platform with 6 Degree-of-Freedom (DoF) rigid body motions, Tran et al. [47] imposed a prescribed sinusoidal pitching motion onto the platform. The unsteady aerodynamic performance of the wind turbine was investigated in response to the various platform motion amplitudes and frequencies using software package STAR-CCM+. By comparing CFD results obtained from STAR-CCM+ with those from other tools, such as unsteady Blade Element Momentum (UBEM), FAST with BEM and Generalized Dynamic Wake (GDW), it was found that although good agreement was achieved for all cases at small oscillation amplitudes, large discrepancies occurred when the oscillation amplitude increased to 4°. This was explained in their work via pointing out the limitations of the simplified methods used in modelling the dynamic interaction between wind turbine and wake, which was induced by the platform motion. As an extension of their work, Tran and Kim [49] analysed an FOWT system under a prescribed sinusoidal surge motion. It is interesting to note that, with the inclusion of the surge motion, the unsteady aerodynamic thrust and power varied considerably among different tools (i.e. FAST, CFD and UBEM), which were also related to the imposed oscillation frequency and amplitude of the surge motion. Li et al. [24] developed an unsteady actuator line model in OpenFOAM and coupled it with a three-dimensional Reynolds-Averaged Navier-Stokes solver to model wind turbine aerodynamics. Numerical modelling on the wake flow of an FOWT experiencing prescribed periodic surge and pitch motions showed the profound effects of platform motions on the aerodynamic performance of the FOWT. More recently, an investigation of Liu et al. [27] on an FOWT with a superimposed three Degrees-of-Freedom (3DoF) platform motion, (i.e. surge, heave and pitch) concluded that the thrust and torque of the wind turbine and thus the power were largely influenced by the motion of the platform.

To well reflect the real situation, a successful analysis of an FOWT, via either CFD simulations or experiment, should consider the complex fluid flow of combined wind and waves. Recently, some researchers have studied the coupled response of a floating offshore wind turbine system under both wind and wave conditions. Ren et al. [36] carried out a CFD analysis of a 5 MW floating wind turbine system supported by a TLP under coupled wave-wind conditions using the commercial software FLUENT with their User Defined Function (UDF). The numerical results were validated against experimental data. It was pointed out that though hydrodynamic forces played a dominant role in the dynamic surge response of a floating system, the aerodynamic forces contributed to the average/mean surge response of the system. Unfortunately, only the surge motion was considered in their study, which obviously simplifies the problem. Quallen et al. [35] performed a full-system, two-phase CFD simulation with an OC3 spar-type FOWT model considering both the wind and wave excitation forces. By comparing CFD results with those from FAST simulations, the predicted mean surge motion with CFD modelling was 25% less than the results from FAST, likely due to a constant drag coefficient adopted in FAST. More recently, Tran and Kim [50] modelled a fully coupled aero-hydrodynamic OC4 semi-submersible FOWT using a dynamic fluid body interaction method coupled with an overset moving grid technique embedded in the commercial CFD software STAR-CCM+. A comparison between the CFD results with FAST data showed overall good agreement. Both codes adopted the quasi-static method for modelling the mooring lines. However, in terms of the maximum wind turbine power, as large as four-fold discrepancy was revealed between the power predicted from the CFD calculations and that from FAST, along with a 32.2% difference in the predicted average mooring tension, indicating the importance of accurate full-system FOWT simulations.

In this paper, we will present a numerical modelling tool based on the open source CFD framework OpenFOAM [34] for fully coupled dynamic analysis of floating offshore wind turbine systems under combined wind-wave excitation. Unlike the previous study by Ren et al. [36] where only the surge degree of freedom was considered, three degrees of freedom responses of the floating structure, which are surge, heave and pitch, are taken into account here while the other three modes of motion (sway, roll and yaw) are ignored. In addition, the effects of the wind speed on the system responses are examined by varying the incoming wind speed. In order to handle the complex mesh movement in an FOWT simulation, a more easily accessible sliding mesh technique is utilised in the present study rather than the overset grid approach employed by Quallen et al. [35] and Tran and Kim [50]. Since a floating wind turbine is a coupled system, the present numerical modelling and data analysis also extend the normally focused aspects to the influences of floating platform motions on the wind turbine aerodynamic performance and vice versa under various wind speed and wave conditions.

In the following, the numerical methods used in the present study are firstly introduced in Section 2. The OC4 DeepCWind semi-submersible floating wind turbine is used for the current investigation and a description about the geometry of the structure is briefly presented in Section 3. In Section 4, validation studies are carried out for different components of the modelling tool. Section 5 shows the results of the dynamic response of the floating system under various working conditions. The results are also discussed in this section. Some conclusions are drawn in Section 6.

2. Numerical methods

2.1. Governing equations

For a transient, incompressible and viscous fluid, flow is governed by the continuity and Navier-Stokes equations:

$$\nabla\cdot\mathbf{U} = 0 \tag{1}$$

$$\frac{\partial\rho\mathbf{U}}{\partial t} + \nabla\cdot\left(\rho(\mathbf{U}-\mathbf{U}_g)\mathbf{U}\right) = -\nabla p_d - \mathbf{g}\cdot\mathbf{x}\nabla\rho + \nabla\cdot\left(\mu_{eff}\nabla\mathbf{U}\right) + (\nabla\mathbf{U})\cdot\nabla\mu_{eff} + \mathbf{f}_\sigma \tag{2}$$

where $\mathbf{U}$ and $\mathbf{U}_g$ represent velocity of flow field and grid nodes, respectively; $p_d = p - \rho\mathbf{g}\cdot\mathbf{x}$ is dynamic pressure of flow field by

subtracting the hydrostatic part from total pressure p; $\mathbf{g}$ is the gravity acceleration vector; ρ is the fluid density; $\mu_{eff} = \rho(\nu + \nu_t)$ denotes the effective dynamic viscosity of fluid, in which ν and ν_t are the kinematic and eddy viscosity respectively; $\mathbf{f}_\sigma$ is a source term due to surface tension which only takes effect at the free surface and equals zero elsewhere.

The two-equation k-ω shear stress transport (SST) turbulence model [29] is employed for the turbulence modelling in this study and the governing equations are:

$$\frac{\partial \rho k}{\partial t} + \nabla\cdot(\rho \mathbf{U} k) = \nabla\cdot(\Gamma_k \nabla k) + \tilde{P}_k - D_k \tag{3}$$

$$\frac{\partial \rho \omega}{\partial t} + \nabla\cdot(\rho \mathbf{U} \omega) = \nabla\cdot(\Gamma_\omega \nabla \omega) + P_\omega - D_\omega + Y_\omega \tag{4}$$

where Γ_k and Γ_ω represent the effective diffusivity of the turbulent kinetic energy k and the specific dissipation rate ω, respectively. $\tilde{P}_k$ and P_ω are the turbulence production terms while D_k and D_ω denote the turbulence dissipation terms. Y_ω is the cross-diffusion term introduced by blending the standard k-ω and k-ε models. Wall functions are adopted for near-wall treatment.

2.2. Free surface capturing

The Volume of Fluid (VOF) method [15] is adopted to capture the free surface between air and water. In this method, a volume fraction variable denoted as α is defined for each cell, representing the ratio of the volume occupied by a certain type of fluid (air or water) in one cell. For a two-phase air-water flow, this variable α complies with the distribution as follows:

$$\begin{cases} \alpha = 0, & air \\ \alpha = 1, & water \\ 0 < \alpha < 1, & free\ \ surface \end{cases} \tag{5}$$

The volume fraction variable α is governed by the following transport equation:

$$\frac{\partial \alpha}{\partial t} + \nabla\cdot\left[(\mathbf{U} - \mathbf{U}_g)\alpha\right] + \nabla\cdot[\mathbf{U}_r(1-\alpha)\alpha] = 0 \tag{6}$$

To better capture the free surface, a bounded compression technique [39] is adopted which introduces an additional third compression term on the left-hand side of the transport equation, where $\mathbf{U}_r$ is a velocity field used to compress the interface [43]. The compression term only functions near free surface due to the inclusion of $(1-\alpha)\alpha$. Coupled with Navier-Stokes equations, the transport equation for the volume fraction is solved to obtain α of each cell and free surface is then determined.

For two-phase flow problems, fluid physical properties, such as density and viscosity, are calculated as weighted averages based on the volume fraction of water and air in one cell as follows:

$$\begin{aligned} \rho &= \alpha\rho_l + (1-\alpha)\rho_g \\ \mu &= \alpha\mu_l + (1-\alpha)\mu_g \end{aligned} \tag{7}$$

where subscripts l and g denote liquid and gas, respectively.

2.3. Wave generation and damping

A wave generation module is incorporated in the present code, which is able to model various types of waves including linear waves, Stokes 2nd order waves, freak waves, solitary waves, etc. [7,41,42]. Numerical waves are generated by specifying the free surface elevation and velocity distribution at the inlet boundary with various wave theories [2], which has been proven to be very effective and the boundary movement is also avoided.

For linear waves, the following equation is used to describe the free surface elevation:

$$\eta = A\cos\theta \tag{8}$$

The horizontal and vertical components of fluid velocity distribution are represented in the equations below:

$$\begin{cases} u = \dfrac{\pi H}{T}\dfrac{\cosh k(z+d)}{\sinh kd}\cos\theta \\ w = \dfrac{\pi H}{T}\dfrac{\sinh k(z+d)}{\sinh kd}\sin\theta \end{cases} \tag{9}$$

where A and $H = 2A$ denote wave amplitude and wave height; T represents wave period; k is wave number; d stands for water depth and $\theta = kx - \omega t$ is the phase.

To alleviate wave reflection from the outlet boundary, a wave damping module is also implemented, which sets up a wave damping zone, i.e. sponge layer [23], near the outlet boundary. The sponge layer takes effect by adding one additional artificial viscous term as a source term to the momentum equation. The new term is thus expressed as:

$$\mathbf{f}_s = -\rho\mu_s\mathbf{U} \tag{10}$$

where μ_s is the artificial viscosity calculated by the following equation:

$$\mu_s(x) = \begin{cases} \alpha_s\left(\dfrac{x - x_0}{L_s}\right)^2, & x > x_0 \\ 0, & x \le x_0 \end{cases} \tag{11}$$

in which α_s defines the damping strength for the sponge layer; x denotes the coordinates of the grid cells in the x direction; x_0 and L_s represent the start position and length of the sponge layer. The artificial viscous term is only effective for those cells inside the sponge layer and is equal to zero elsewhere.

2.4. Mooring line modelling

For floating structures, mooring systems are of great importance, especially for those three DoF motion responses (surge, sway and yaw) where the hydrostatic restoring forces/moments are not present. In order to model the mooring system for the FOWT, a quasi-static mooring line analysis model is integrated into the solver in the present study. In this model, a mooring line is divided into a given number of segments with identical length [11,26]. For each segment, equations of static equilibrium are established in both horizontal and vertical directions as shown in Fig. 1:

$$\begin{cases} T_{x(i+1)} = T_{xi} \\ T_{z(i+1)} = T_{zi} + w_i dl \end{cases} \tag{12}$$

Geometric constraint is also considered for node coordinates and stretched length:

$$\begin{cases} ds\cos\varphi_{i+1} = x_i' - x_{i+1}' = \Delta x' \\ ds\sin\varphi_{i+1} = z_{i+1}' - z_i' = \Delta z' \end{cases} \tag{13}$$

In addition, the tension force acting on the segment is linked to the elongation in the following way:

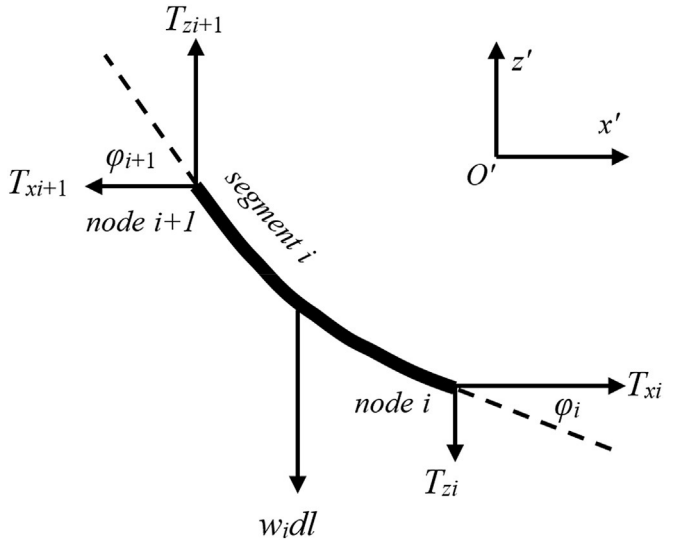

Fig. 1. Sketch of segment i in the static mooring line analysis model.

$$ds = dl\left(1 + \frac{T_{i+1}}{EA}\right) \tag{14}$$

where T_x and T_z represent the horizontal and vertical components of total tension T at one of the nodes of the segment; w is net submerged weight of the segment per unit length; dl and ds are the length of the segment before and after elongation respectively; φ is the angle between T and T_x; E and A denote the Young's modulus and cross-sectional area for the segment separately.

At the beginning of every time step, the tension components at the fairlead are firstly estimated using the value from the last time step, and then solved using the secant method in an iterative manner. The interaction between the mooring line and the seabed is handled by a kinematic constraint. The tension is subsequently applied to the floating structure at the fairlead as an external mooring loading.

2.5. Body movement and mesh motion handling

One of the biggest challenges in numerical modelling of a fully coupled FOWT system is how to handle the mesh motion to represent the complex body movement involved. For an FOWT system, the wind turbine blades rotate around its hub, which also moves along with the supporting platform in six degrees-of-freedom. Currently, one of the common practices to deal with such problems is to employ an overset or Chimera grid technique [35,50], where a system of multiple layers of disconnected component grids overlapping each other is used to discretise the flow domain. The overset grid is undoubtedly rather powerful and suits the FOWT applications quite well. However, it is not easily accessible due to various reasons. For example, to access commercial CFD software packages with the overset grid capability such as STAR-CCM + used by Ref. [50], a license has to be obtained. On the other hand, for some in-house codes like the CFDShip-Iowa [35], the FoamedOver library [6] and the naoe-FOAM-SJTU solver implemented in OpenFOAM [44], either the commercial overset grid assembly software SUGGAR or an improved version Suggar++, which is intended to generate the domain connectivity information (DCI), also requires the costly licence keys.

In this work, a built-in sliding mesh technique in OpenFOAM termed AMI (Arbitrary Mesh Interface) is adopted to cope with the relative motion problem in FOWT applications instead of developing a complex overset grid approach. The AMI method is designed for rotating machinery problems, which allows simulations across disconnected but adjacent mesh domains either stationary or moving relative to one another [32]. Geometrically, two cylindrical AMI sliding mesh surfaces are generated as shown in Fig. 2, an inner small one for the rotating wind turbine and an outer large surface surrounding the whole system. Since the upper wind turbine may also undergo a pitching motion, the outer sliding mesh surface is extended to completely cover the turbine and the platform. The axis of the inner cylindrical surface coincides with the rotation axis of the wind turbine, while the axis of the outer surface points through the system's mass centre and is perpendicular to the wave propagation direction. In the present study, we only consider three free DoF FOWT motion responses, i.e. surge, heave and pitch, and they all lie in the same XoZ plane. Thus, a cylindrical outer sliding mesh surface (see Fig. 2) is sufficient to represent the rigid body motion. However, when all six DoF motion responses are investigated, a more versatile spherical topology has to be applied.

The whole computational domain is split into three cell zones via the aforementioned two sliding mesh surfaces as sketched in Fig. 3, i.e. the inner cell zone in black, the middle cell zone in grey and the outer cell zone in white. The multiSolidBodyMotionFvMesh dynamic mesh motion library is selected to apply different mesh motions to different cell zones. When the floating system is in motion, the outer zone only translates in the surge and heave directions thus the inlet and outlet boundaries remain vertical. The middle zone may experience pitch motion as well as surge and heave, while the inner zone undergoes all three DoF motion together with the prescribed rotation of the wind turbine. The strategy of separating the whole domain into several cell zones with their specific mesh motions without the utilisation of an overset mesh makes it possible to perform a full-system analysis for an FOWT in an easy and more accessible way. Apart from the moving mesh strategy we apply herein, it is worthwhile to mention that the method adopted by Ren et al. [36], where a sliding mesh technique was combined with a dynamic mesh morphing algorithm, is another approach to handle the relative mesh motion problem in FOWT applications without the need of the overset grid technique.

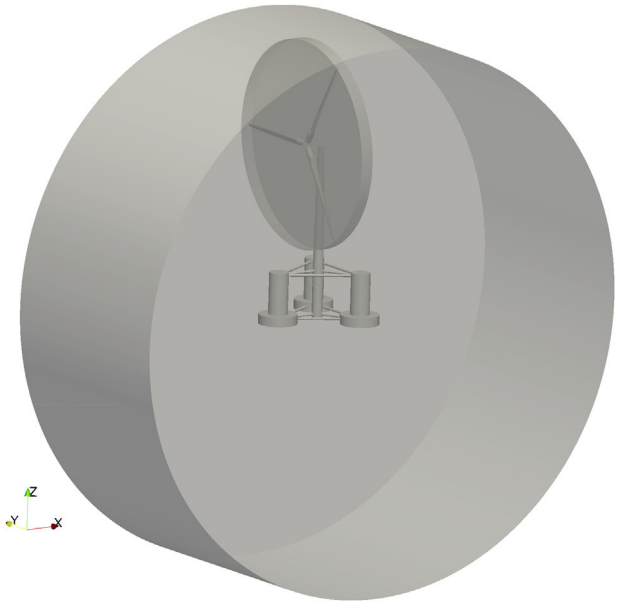

Fig. 2. AMI surfaces of the floating wind turbine.

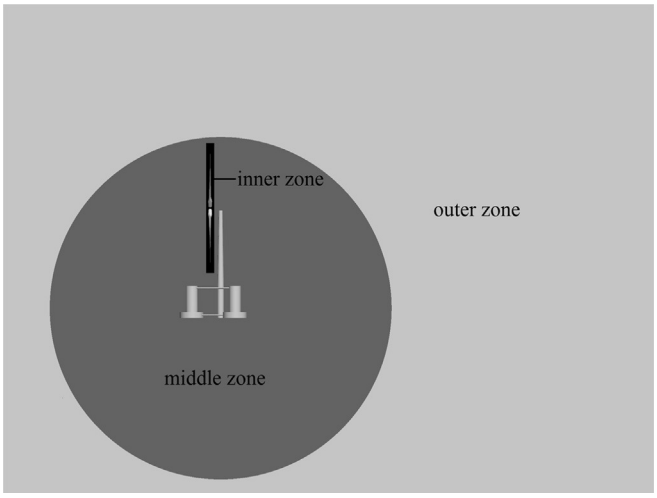

Fig. 3. Cell zones of the floating wind turbine.

2.6. Modelling procedure

In order to solve the fully coupled fluid-structure interaction problem, a coupled calculation procedure is adopted as follows. As can be seen from the illustrative flow chart in Fig. 4, when a simulation starts, the flow field is initialised first. At the beginning of every time step, both the aerodynamic and hydrodynamic loadings are integrated over all the surfaces of the floating system including the turbine, tower and the supporting platform. The loadings from the mooring system are also calculated using the position and orientation of the floating system from the last time step or iteration. The motion responses of the floating system are then obtained by solving a set of motion equations using the second-order method adopted by OpenFOAM. The computational mesh is subsequently updated using the predicted system motion responses, and the Navier-Stokes equations are solved together with the equations related to the volume fraction variable and turbulence variables. The flow field convergence is checked at the end of every iteration. If it has not converged, a new iteration begins; otherwise, the computation advances to the next time step.

3. Model description

A semi-submersible floating offshore wind system (Fig. 5) studied in the Phase II of the Offshore Code Comparison Collaboration Continuation (OC4) project is investigated in the present work. The whole system consists of the NREL 5-MW baseline wind turbine designed for offshore applications [21], the OC4 tower, the OC4 DeepCWind semi-submersible [37] supporting the tower and the mooring system. In this section, descriptions of the floating offshore wind system are presented.

In 2011, a series of model tests on a 1/50th-scale semi-submersible FOWT was carried out at Maritime Research Institute Netherlands' (MARIN's) offshore wind/wave basin, aiming to calibrate and validate the currently available FOWT modelling tools, such as FAST [8,38]. Although the geometry defined in the report published by Ref. [37] was adopted in the tests, some adjustments were made during the fabrication process. Details about the geometry definition can be found in the work published by Coulling et al. [8] and the major discrepancies between the data from NREL's reports and those used in the tests in terms of gross properties are compared in Table 1. It was noted that all published data represented are associated with a full-scale device. The parameters and

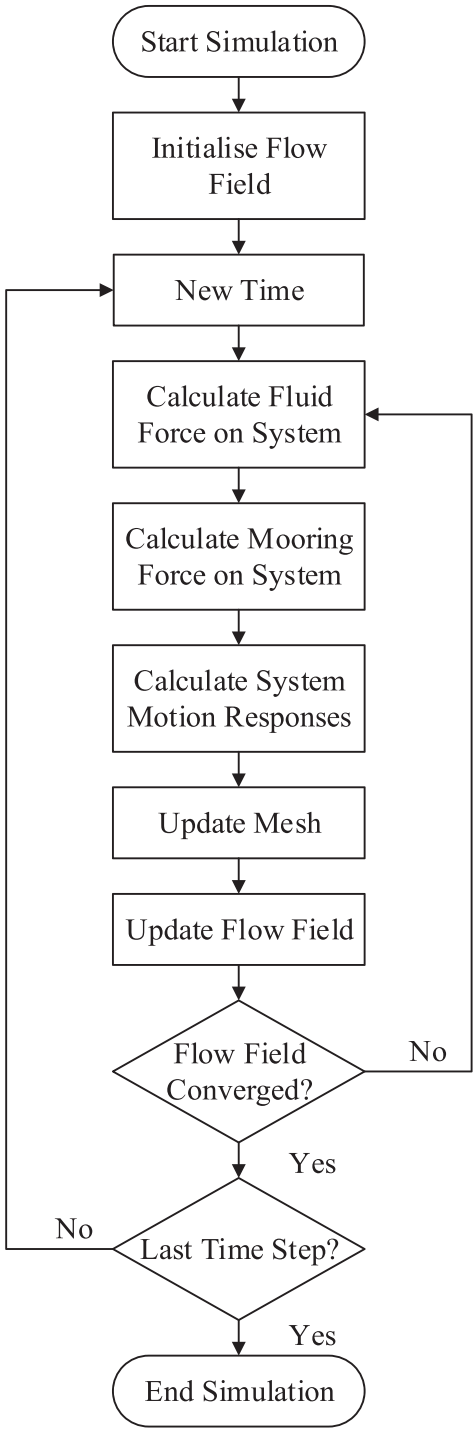

Fig. 4. Calculation procedure for the coupled analysis.

gross properties used in the model tests are employed in the present work so that validation could be made against model test data.

An important change for the wind turbine model used in Coulling's tests was that both the shaft tilt angle and pre-core angle were set to zero as the turbine blades were designed to be almost rigid. As a result, the potential aero-elasticity of the blades could be neglected. Other variations are mainly in relation to the mass and inertia properties of various parts of the system. For example, the mass of a blade was decreased from 17,740 kg to 16,450 kg in the tests, possibly due to the material and fabrication reasons. The CAD

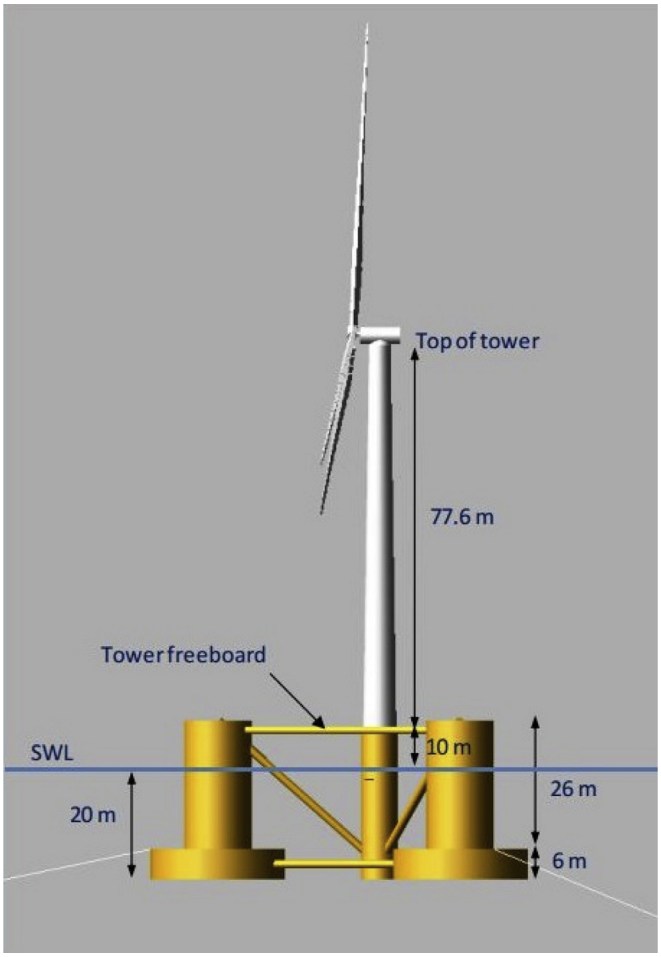

Fig. 5. Sketch of the semi-submersible floating offshore wind system [37].

model of the wind turbine is created using the blade model file published by Hsu [17] and is illustrated in Fig. 6. The turbine rotor hub connecting the three blades and the nacelle are not modelled for simplicity.

Since the motion responses of an FOWT need to be solved as an entire system when performing a dynamic analysis, the mass and inertia properties of the system must be determined in advance as listed in Table 3. Properties for the mooring system remain the same in the model tests as those published by Ref. [37] and are reproduced in Table 2. The layout of the mooring system composed of three mooring lines is sketched in Fig. 7.

4. Validation of modelling methodologies

As a floating offshore wind turbine is a rather complex system, the validation of our developed numerical model is performed for three parts individually, i.e. the aerodynamic performance of a fixed wind turbine, the restoring force of a mooring system and the hydrodynamics of a floating platform.

4.1. Aerodynamics of a wind turbine

The NREL Phase VI wind turbine, rather than the NREL 5-MW offshore wind turbine, is adopted in this section to validate the numerical modelling of the wind turbine aerodynamic performance. Though the NREL Phase VI wind turbine was initially designed for the applications under onshore scenarios, the availability of experimental data [13] from NREL makes it a popular benchmark case in the research area of wind turbines.

The NREL Phase VI wind turbine is a two-bladed upwind model

Fig. 6. CAD model of the NREL 5-MW wind turbine.

Table 1
Comparison between data published by NREL and those used in MARIN's model tests.

Gross properties	NREL	MARIN
Overhang, shaft tilt angle and pre-cone angle of wind turbine	5 m, 5°, 2.5°	10.58 m, 0°, 0°
Blade mass	17,740 kg	16,450 kg
Blade second mass moment of inertia	11,776,047 kg m^2	13,940,000 kg m^2
Nacelle mass	240,000 kg	274,940 kg
Nacelle pitch inertia	Not specified	22 440 000 kg m^2
Hub mass	56,780 kg	72,870 kg
Total tower-top mass	350,000 kg	397,160 kg
Tower mass	249,718 kg	302,240 kg
Center of mass (CM) above SWL (still water level) for tower	43.4 m	44.6 m
Platform mass, including ballast	13,473,000 kg	13,444,000 kg
CM location below SWL along platform centreline	13.46 m	14.4 m
Platform roll inertia about CM	6.827×10^9 kg m^2	8.011×10^9 kg m^2
Platform pitch inertia about CM	6.827×10^9 kg m^2	8.011×10^9 kg m^2
Platform yaw inertia about platform centreline	1.226×10^{10} kg m^2	1.391×10^{10} kg m^2

Table 2
Gross properties of the mooring system.

Number of mooring lines	3
Angle between adjacent lines	120°
Depth to anchors below SWL (water depth)	200 m
Depth to fairleads below SWL	14 m
Unstretched mooring line length	835.5 m
Mooring line diameter	0.0766 m
Equivalent mooring line mass in water	108.63 kg/m
Equivalent mooring line extensional stiffness	753.6 MN

and each blade adopts the NREL S809 airfoil profile as shown in Fig. 8 (a) at the most of its span-wise cross sections. The length of the blade is 5.029 m from tip to the rotation axis. Of all the configurations tested by NREL, a tip pitch angle of 3° is used and zero yaw angle is applied in the present study. Fig. 8 (b) displays a CAD model for the wind turbine. As is seen from the figure, we exclude the hub, nacelle and tower parts to make our numerical model simple. Detailed geometric parameters can be found in the NREL report [13].

Fig. 9 shows the overall computational domain, i.e. a cylindrical domain with a diameter of 5D, where D is the diameter of the rotor. The inlet and outlet boundaries are 1.5D and 4D away from the rotor, respectively. The rotational motion of the wind turbine is handled by the aforementioned AMI sliding mesh technique. The rotor is surrounded by a small cylindrical domain and the faces connecting the two domains are defined as the AMI sliding interfaces. To model a fixed wind turbine, the inner small cylinder region (or rotor region) rotates around a predefined axis while the outer domain (or stator region) maintains static. The built-in snappyHexMesh utility in OpenFOAM is adopted for mesh generation. This utility is very powerful yet easy to use and capable of generating hexahedra dominant mesh [33]. An illustration of the overall computational mesh can be seen in Fig. 10 as well as the detailed sectional view of the mesh near the turbine blade. Four different incoming wind velocities, i.e. 5, 10, 15 and 25 m/s, are investigated and the rotational speed of the turbine rotor is fixed at 72 RPM.

Table 3
Gross properties of floating offshore wind system.

Total mass of the system	14,143,400 kg
System CM location below SWL along platform centreline	10.20754 m
Roll inertia about system CM	1.31657×10^{10} kg m^2
Pitch inertia about system CM	1.31657×10^{10} kg m^2
Yaw inertia about platform centreline	1.90647×10^{10} kg m^2

4.1.1. Thrust and torque

Thrust and torque are two important aerodynamic performance parameters for a wind turbine as they represent the integral loading on the turbine. Thrust is defined as the integrated force component normal to the rotor plane while torque is the integrated moment component parallel to the rotating axis of the wind turbine as defined in the following equations:

$$\begin{aligned} T &= \oint_S p\mathbf{n}\cdot\mathbf{dS} \\ Q &= \oint_S (\mathbf{r}\times p\mathbf{n})\cdot\mathbf{dS} \end{aligned} \tag{15}$$

where **dS** is the area vector of an infinitesimal surface, **n** is the direction vector normal to the rotor plane (pointing in the downwind direction) and **r** is the distance vector from the rotation centre to the surface.

Due to the unsteadiness caused by the rotational motion of blades, both thrust and torque vary with time. The results presented here are obtained by averaging the time history curves over a certain rotation period. A comparison between the present results and data obtained from the NREL report [13] is demonstrated in Fig. 11. The vertical bars in the figures represent the experimental standard deviation. Numerical results through CFD simulation by Li et al. [25] are also plotted for comparison. As is seen from the

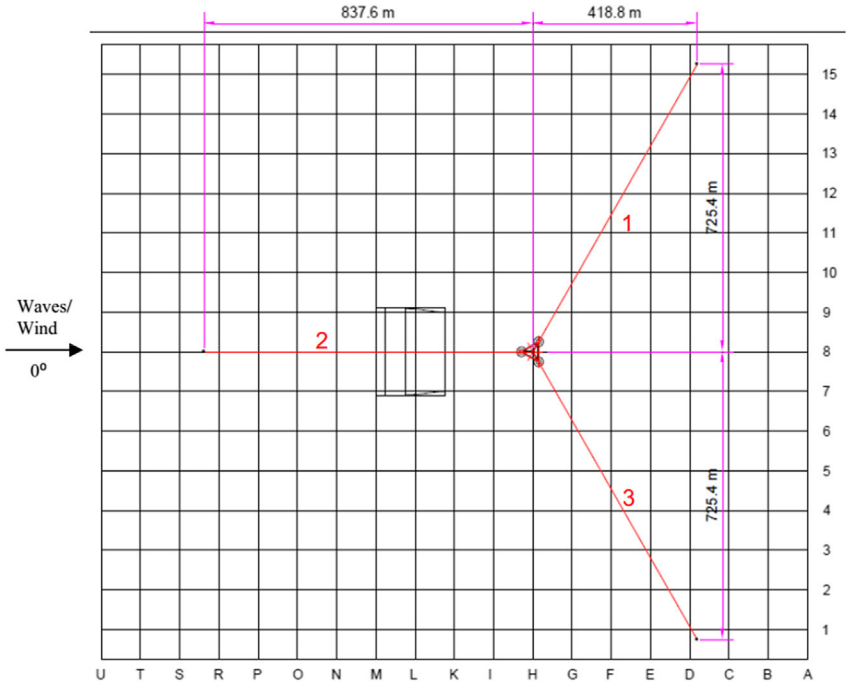

Fig. 7. Layout of the mooring system [37].

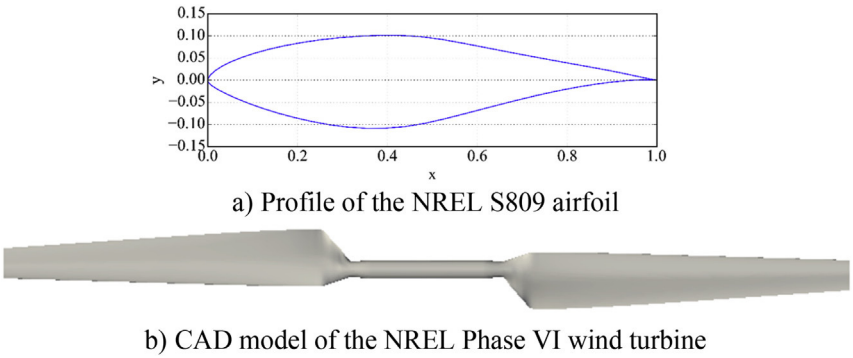

Fig. 8. Geometry of the NREL Phase VI wind turbine.

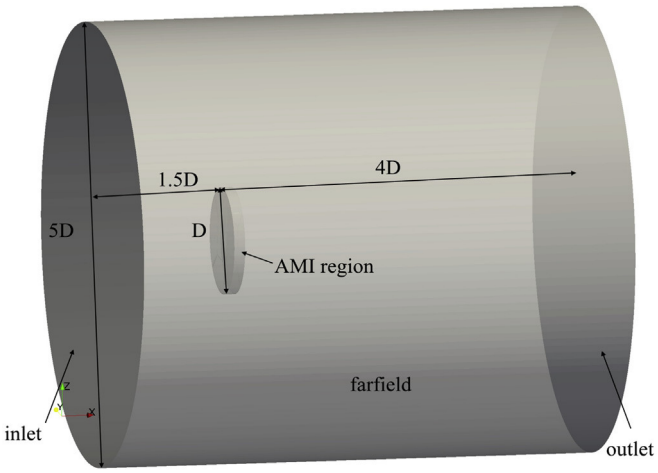

Fig. 9. Computational domain for the NREL Phase VI wind turbine.

figures, an overall good agreement is achieved for the present results and the experimental data, except for an over-prediction of 11% in thrust at a wind speed of 25 m/s, where stalled flow and separation are significant, thus difficult to predict accurately. In addition, both our calculated thrust and torque agree well with those from Li's paper, indicating the capability of present CFD solver for modelling wind turbine aerodynamics.

4.1.2. Pressure coefficients

Pressure coefficient can reflect flow information in a more detailed manner than the thrust and torque. It is defined as:

$$C_p = \frac{P_0 - P_\infty}{0.5\rho\left[U^2 + (\omega r)^2\right]} \tag{16}$$

where P_0 is the measured pressure at a given location; P_∞ is the reference pressure in the far field and is zero in this case; U stands for the wind velocity; ω is the rotational speed and r denotes the distance between the section of the specified location and the rotation centre.

Fig. 12 shows the comparison between our CFD predicted and NREL experimentally measured pressure coefficients at three cross sections for four different wind velocities. As can be seen from the figures, the predicted pressure coefficients agree quite well with the experimental data for four wind conditions. Although some discrepancies are notable at the incoming wind velocity of 15 m/s, similar differences were also observed by Li et al. [25] and Hsu et al. [16].

4.2. Mooring restoring force

In order to validate the quasi-static mooring line analysis module adopted in the present study, a series of numerical tests is carried out with the mooring system. The fairleads of all the three mooring lines are translated in surge and sway DoF from −20 m to 20 m, and the predicted total restoring force from the mooring system is compared to both experimental data and results from FAST's quasi-static mooring module reported in the work of Coulling et al. [8]. Comparison shown in Fig. 13 demonstrates that the results from present simulation agree very well with experimental

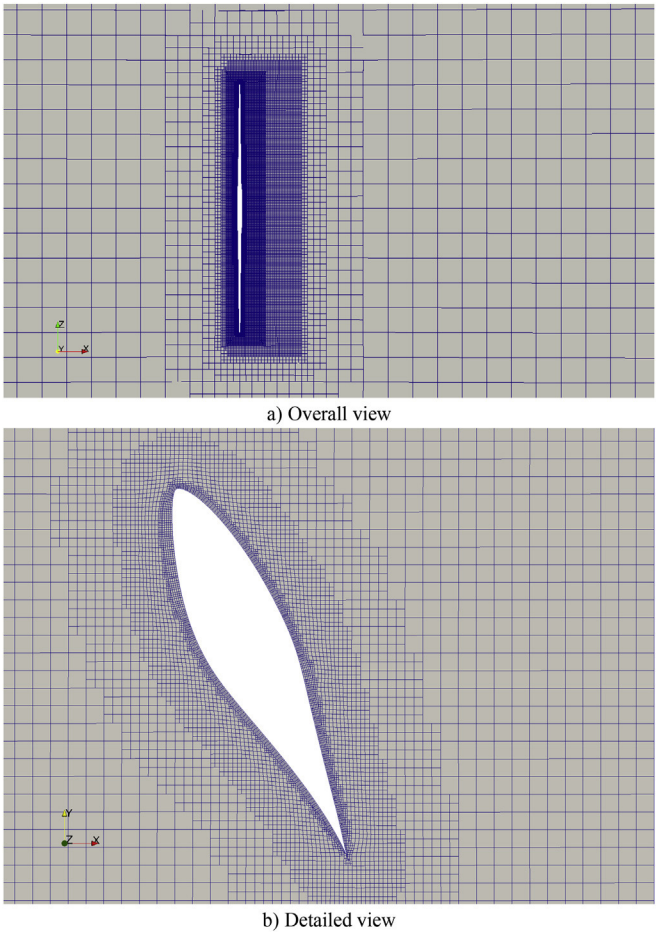

Fig. 10. Computational mesh for the NREL Phase VI wind turbine.

data, indicating the current mooring line analysis module is capable of predicting the static characteristics of a mooring system.

4.3. Hydrodynamics of a floating platform

The hydrodynamic module of the present numerical modelling tool is validated against the data from MARIN's model tests [8]. A series of cases involving different environmental conditions was considered in the model test for the OC4-DeepCWind Semi-submersible, while only free decay tests and motion response under regular waves are studied in the current work as part of our validation tests.

4.3.1. Free decay tests

Free decay tests are usually performed in a wave tank to determine the natural period of a floating system. The three DoF motion responses (surge, heave and pitch) of great significance in head wave conditions are tested in the present study. It is worth mentioning that the present simulations also take into account an additional surge stiffness of 7.39 kN/m, which was provided by the cable bundle used to transmit data from the floating system to the computers in the model tests, and was estimated using the free decay model test data [8].

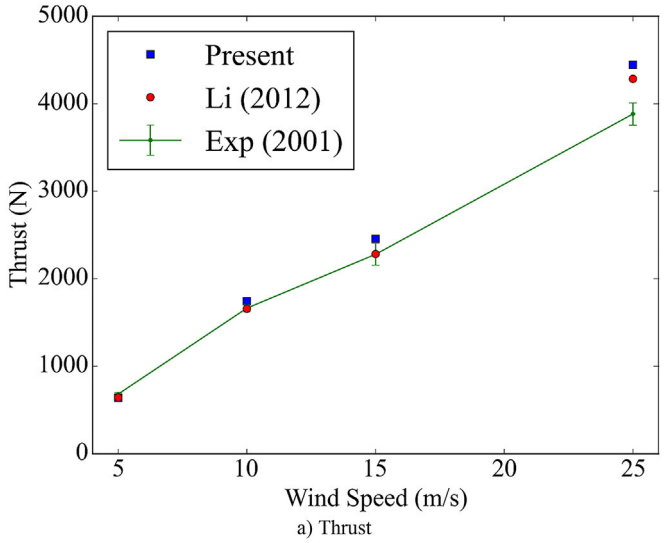

Fig. 11. Comparison of thrust and torque with available experimental and numerical results.

The natural periods of the three DoF motion responses from the present simulations are summarised in Table 4. It is seen that comparison of the present results to experimental data and the results from FAST and other CFD simulations [48] reveals good agreement. Besides natural periods, damping ratios can also be obtained from free decay tests, which are of equal importance for an accurate prediction of the dynamic motion responses of a floating system. Fig. 14 (a) demonstrates the heave free decay response of the floating system with an initial heave displacement of 3 m. Damping ratios are calculated with two consecutive amplitudes, indicated as the square markers in Fig. 14 (a). Fig. 14 (b) shows the heave damping ratios over the initial cycle amplitude in the free decay test. It is obvious that the results predicted by the present CFD tool are in good agreement with other published data.

4.3.2. Hydrodynamic response under regular waves

The hydrodynamic responses of the floating system under regular waves are also simulated. In this study, no aerodynamic forces are considered and the upper wind turbine is not modelled. The regular wave under study has a wave amplitude of 3.79 m and a wave period of 12.1 s. To exclude the effects of disturbance from the initial start-up stage, simulation runs for 400 s to achieve a nearly periodic quasi-steady state. Surge, heave and pitch motion amplitudes are estimated by averaging the amplitudes within the last eight wave periods. These values are then normalised by the amplitude of the regular wave to obtain the response amplitude operator (RAO).

To deal with the movement of the platform, the AMI sliding mesh technique mentioned earlier is adopted by creating a cylindrical region surrounding the platform so that the pitching motion is achieved by rotating the AMI region as shown in Fig. 15. The centre of the region is located at the centre of rotation of the platform, which in this case coincides with the mass centre of the floating system listed in Table 3. The surge and heave motions, however, are represented by the solid body motion of the whole computational domain including the AMI domain, which avoids the deterioration of mesh quality due to mesh deformation commonly used in the applications involving body movements.

Three sets of mesh with different grid density are created to ensure that mesh-insensitive results are obtained. Fig. 16 shows a medium-sized mesh for the floating platform, where the mesh is clustered near the free surface and the platform. Eight layers of boundary layer cells are extruded from the platform surface with a growth ratio of 1.2 and the first cell height away from the surface is 0.012 m. Table 5 summarises the estimated RAOs for three sets of mesh, where the percentage difference over data obtained with fine grid is also included. A maximum deviation of −3.42% indicates that the results are mesh-independent. Therefore, a medium grid is applied for later comparison and simulation.

A comparison is also made and illustrated in Fig. 17 for the motion RAO results from the medium grid with the model test data and those from FAST [8] as well as other CFD simulations [50]. The present CFD simulations predict similar RAOs in response to other data under the regular wave conditions. The time history curves for the three DoF are also plotted in Fig. 18. It should be noted that the mean heave motion is below zero due to the imbalance between the gravity force and the calculated vertical mooring loading of the floating system and the buoyancy force predicted by integrating pressure along the discretised surface. The surge motion also has a mean value of 0.8686 m because of the drift force in waves.

The mooring line tensions for lines #1 and #2 defined in Fig. 7 are plotted in Fig. 19. It is clear that both the mean and peak tensions for line #2 in the head wave direction are larger than for line

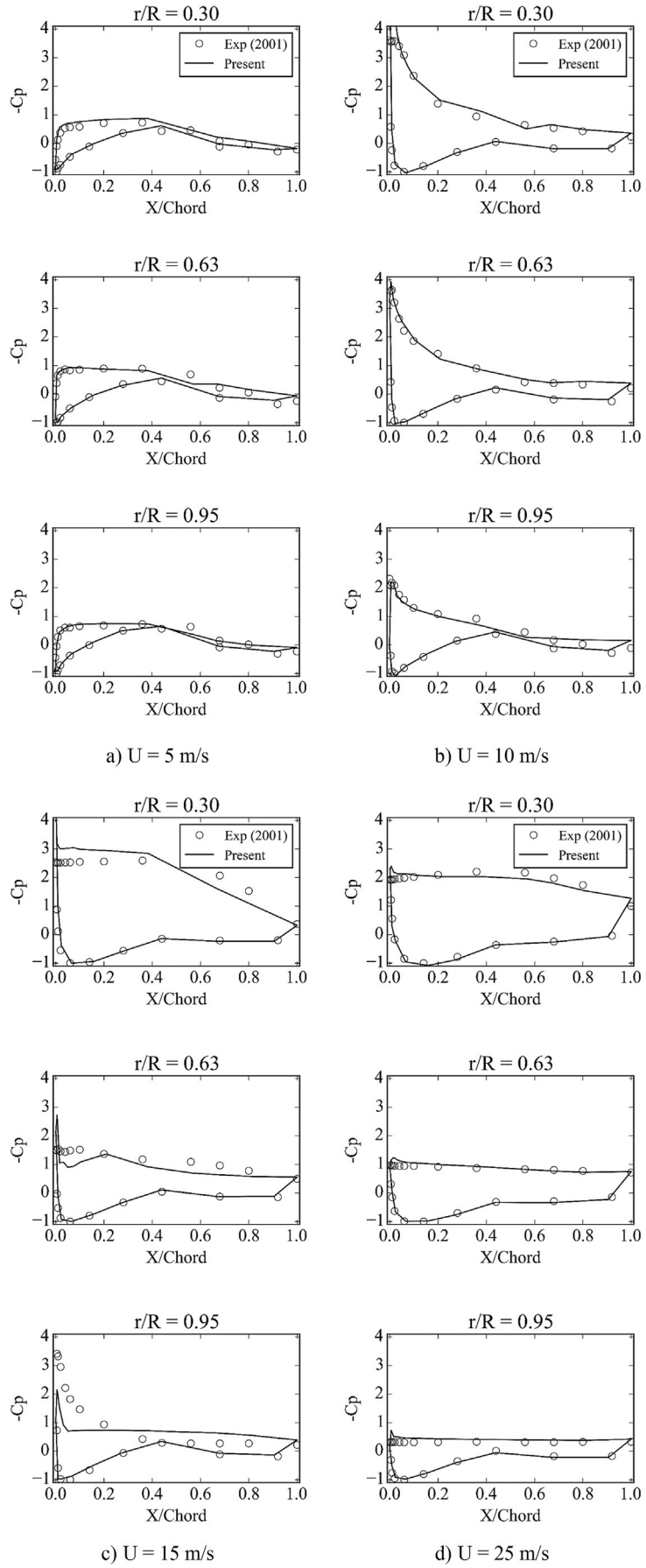

Fig. 12. Pressure distribution along blade at different wind velocities ('-' represents the negative sign).

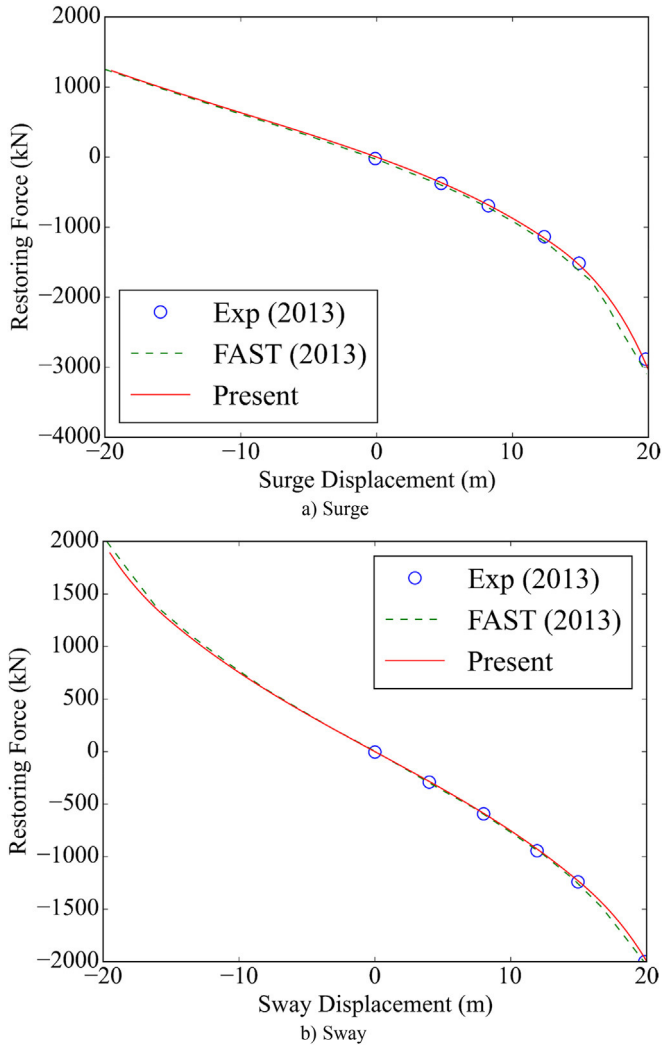

Fig. 13. Comparison of surge and sway mooring restoring force.

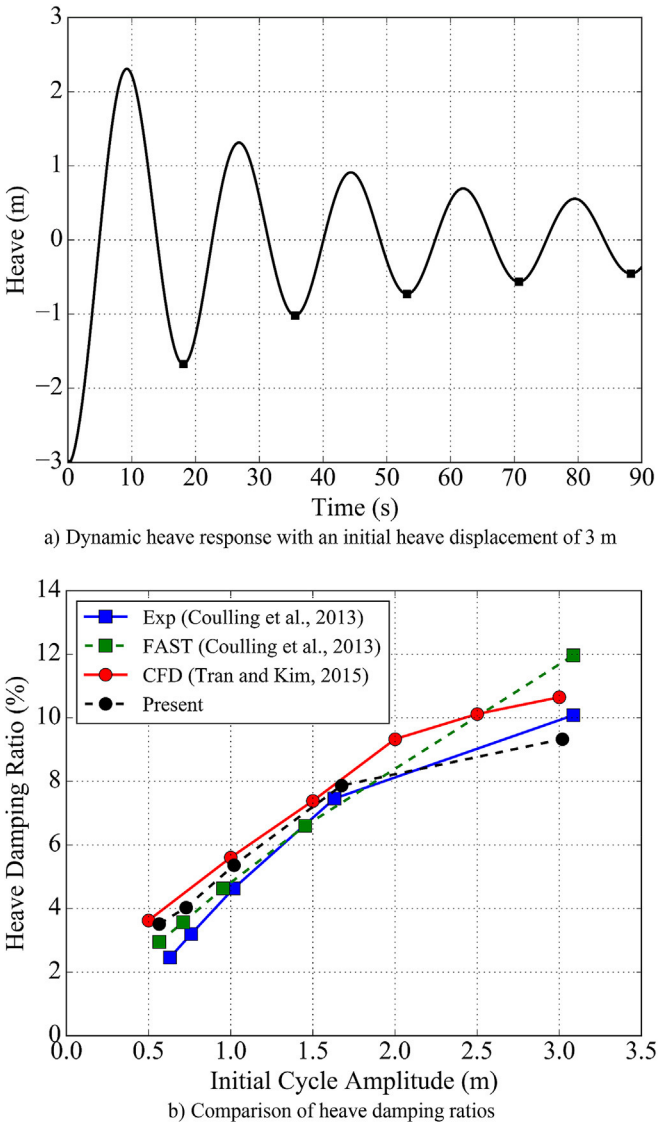

Fig. 14. Heave free decay simulation results.

#1 in the back wave direction due to the drift force. A mooring line tension RAO is defined by normalising the tension amplitude with the incident wave amplitude. Fig. 20 shows the comparison of present results with other experimental and numerical data. Good agreement is observed between the results obtained from three numerical simulations based on different tools, although they all significantly under-predict the line tensions for both lines compared to the experiment. The discrepancy might result from the application of a static mooring analysis model rather than a dynamic model in all three simulations. This phenomenon was also noted in the work of Coulling et al. [8] and Tran and Kim [50], which gives an indication that a more accurate dynamic mooring model should be adopted in the future study as suggested by the investigation of Masciola et al. [12], Hall and Goupee [28] and Antonutti et al. [1]. Nevertheless, the platform motion RAOs do not seem to be largely affected due to this static mooring model used in the present study, and therefore it is reasonable to conclude the

Table 4
Comparison of natural periods of floating system from free decay tests (Unit: s).

DoF	Exp [8]	FAST [8]	CFD [50]	Present
Surge	107	107	108.1	107.2
Heave	17.5	17.3	17.8	17.5
Pitch	26.8	26.8	25.2	27.4

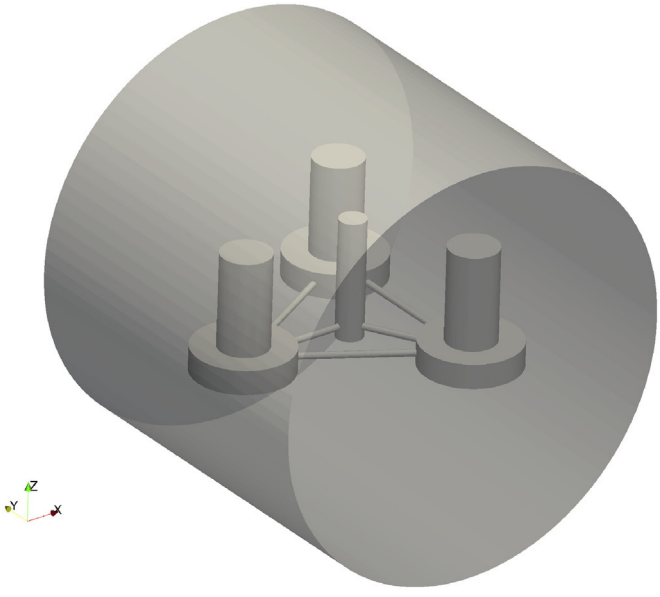

Fig. 15. AMI domain surrounding the floating platform.

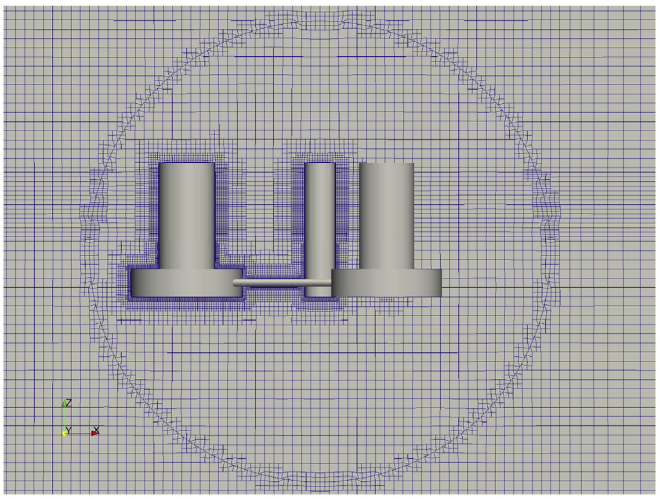

a) Overall view

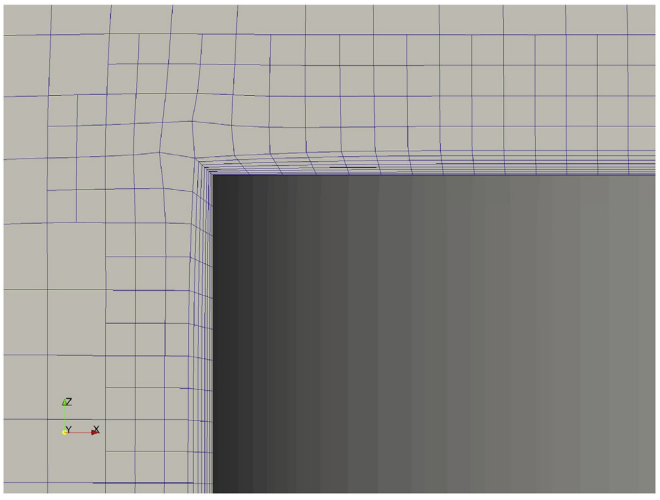

b) Detailed view near the base column

Fig. 16. Mesh for the floating platform.

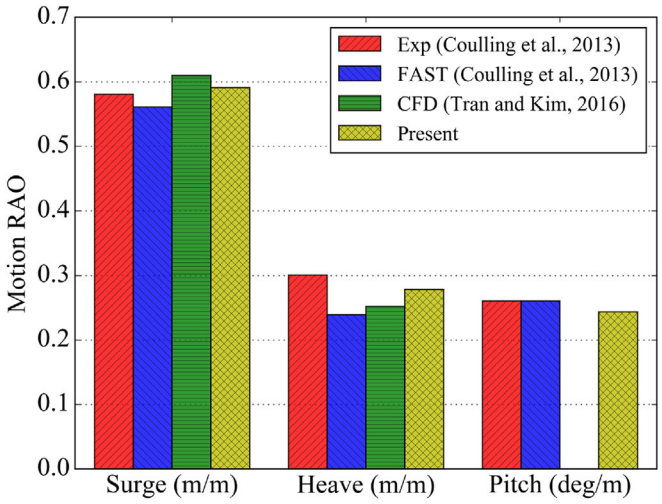

Fig. 17. Comparison of RAO for surge, heave and pitch responses.

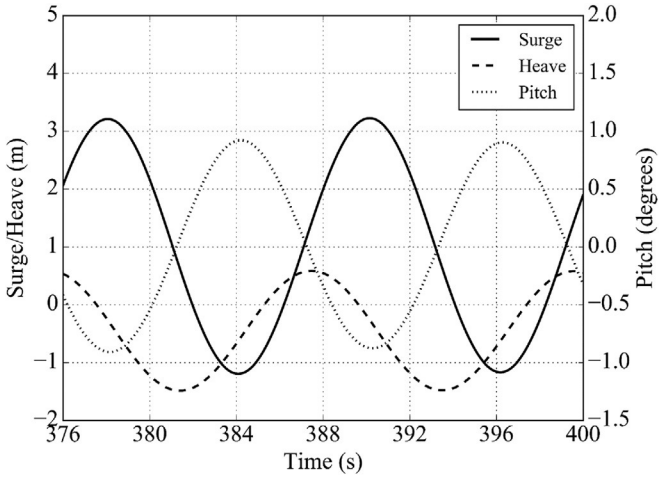

Fig. 18. Time history curves for the floating platform under regular waves.

applicability of using the static mooring model to predict platform motion responses in FOWT simulations.

5. Results and discussion

5.1. Aerodynamics of the NREL 5-MW wind turbine

The aerodynamics of the NREL 5-MW fixed wind turbine is firstly studied in full scale without the floating platform and will be used for later comparison with the data of a floating wind turbine. One specific operating condition taken from Coulling et al. [8] is selected. The incoming wind speed is 7.32 m/s, and the turbine rotor rotates at a speed of 4.95 RPM with a collective blade pitch angle of 6.4°.

Three sets of grid are generated with different grid density while all other parameters remain unchanged. The medium-sized mesh of the wind turbine is shown in Fig. 21. The regions near the blade tips and blade roots are intentionally refined to better capture the tip and root vortices. Eight layers of boundary layer cells are extruded from the turbine surface with a growth ratio of 1.2 and the first cell height away from the turbine surface is 0.004 m.

Fig. 22 shows the aerodynamic thrust and torque from three sets of mesh. To eliminate the initial start-up effects, the thrust and torque are averaged from 20 s to 30 s to obtain time-averaged values, which are then listed in Table 6. Results are also presented in percentage difference over data obtained with fine grid. It can be clearly seen that the difference for both thrust and torque between medium and fine mesh is below 1%, indicating that the results are insensitive to the grid number. Thus, the medium mesh is selected for later simulation to balance the computational accuracy and the

Table 5
Mesh-sensitivity test for RAO of floating platform under regular waves (percentage in parentheses shows the difference over data obtained with fine grid).

Grid	Cell Number (in million)	Surge (m/m)	Heave (m/m)	Pitch (°/m)
Coarse	2.35	0.5982 (−1.56%)	0.2878 (−1.44%)	0.2442 (−3.21%)
Medium	3.14	0.5965 (−1.84%)	0.2820 (−3.42%)	0.2470 (−2.10%)
Fine	4.55	0.6077 (−)	0.2920 (−)	0.2523 (−)

computing time needed to complete the calculation.

5.2. Effects of the floating platform on wind turbine aerodynamics

In order to study the influence of the floating platform imposed upon the aerodynamics of the wind turbine, a fully coupled CFD simulation is carried out for the OC4 FOWT in full scale. In this section, we will analyse the aerodynamic thrust and torque of the wind turbine and compare them with any available data.

Fig. 23 illustrates the cross-sectional view of the mesh at the xoz plane. Mesh refinement is applied near the free surface as well as in the vicinity around turbine blade tip and root vortex regions. Nearly 10 million cells are generated using the built-in snappyHexMesh utility in OpenFOAM.

The environmental conditions are the combinations of the aforementioned regular waves and steady wind, which are summarised in Table 7. Two cases are set up where the wave parameters remain the same while two different wind speed and rotation speed configurations are adopted to study the impacts imposed by wind speed. In Case #1, the wind speed is 7.32 m/s and the rotation speed is 4.95 RPM, the same as in Section 5.1. In Case #2, the steady wind speed is 11 m/s and the rotation speed is 11.89 RPM, which is closer to the rated operating condition of the NREL 5-MW wind turbine and thus can better reflect the system responses under design operating conditions. The wind condition in Case #2 is exactly the same as that in the work of [50], which makes it possible to compare relevant results from two different CFD codes as shown in Table 8.

To exclude the effects of disturbance from the initial start-up stage, simulation was carried out for 350 s to achieve a nearly periodic quasi-steady state. During the simulations, the aerodynamic thrust and torque of the FOWT are recorded and results over the last four periods are used for further data analysis. Both thrust and torque are translated to the local wind turbine coordinate system so that they are consistent with the definition in Eqn. (15) and can be compared with the data from the fixed turbine simulation in Section 5.1. A comparison of the aerodynamic thrust and torque is made for the floating wind turbine simulation and the fixed turbine simulation in Case #1 and is illustrated in Fig. 24 (a), where the data from fixed turbine is extracted from the case with a medium mesh density.

It is easily seen from Fig. 24 (a) that the instantaneous thrust and torque are time dependent due to the motion of the floating platform, while the time-averaged thrust and torque are quite similar to those from the fixed turbine simulations. Table 8 summarises the

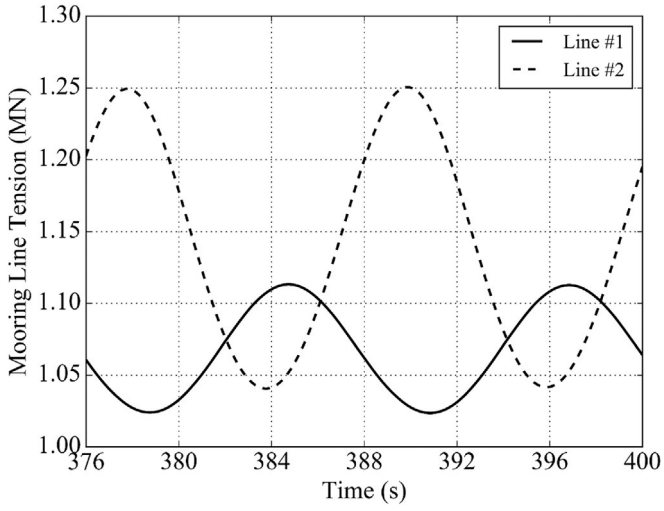

Fig. 19. Time history curves for mooring line tension of lines #1 and #2 under regular waves.

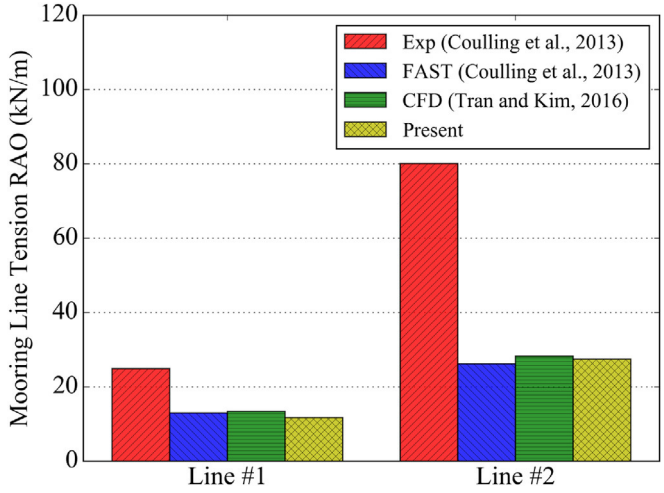

Fig. 20. Comparison of tension RAO for mooring lines #1 and #2.

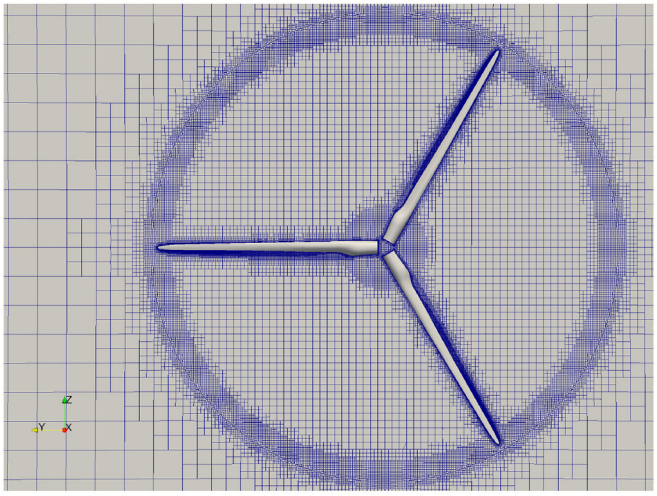

a) Overall view

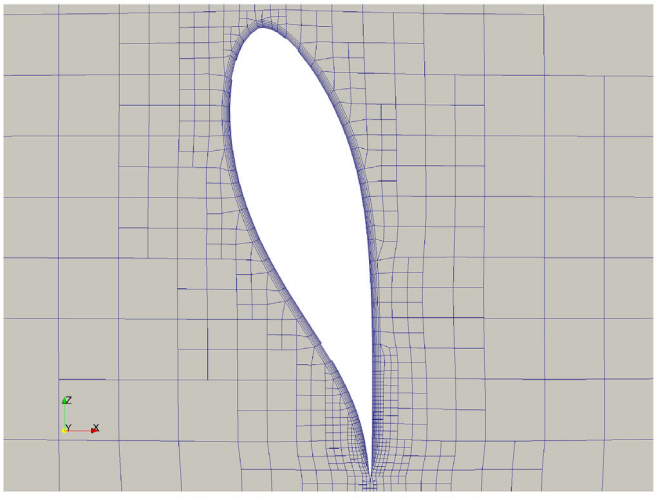

b) Detailed view near the turbine blade

Fig. 21. Mesh for the NREL 5-MW wind turbine.

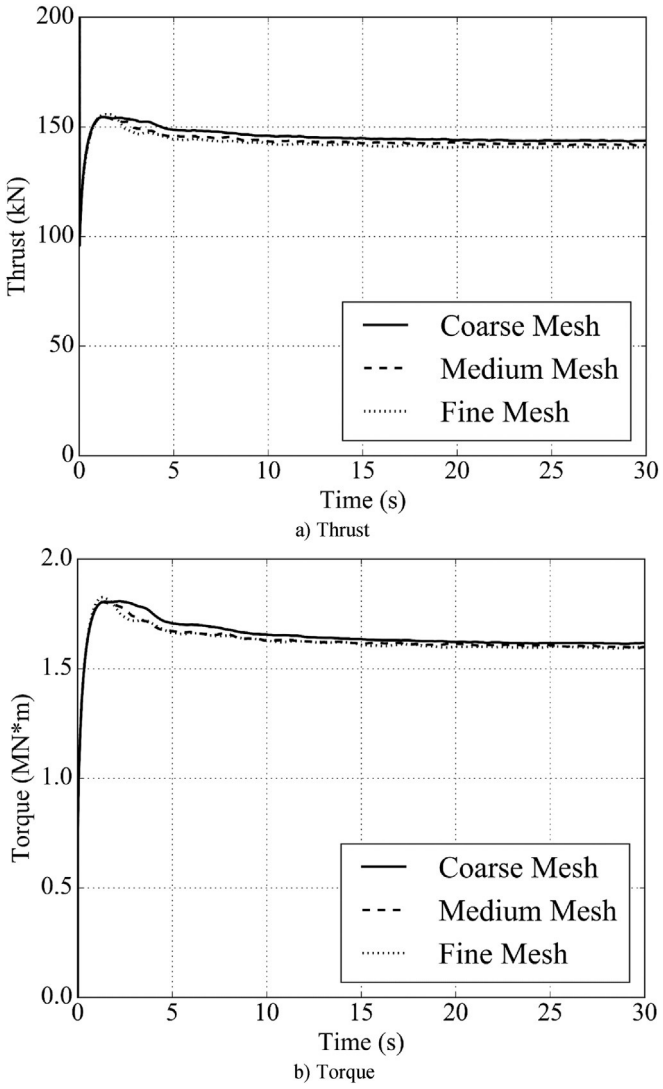

Fig. 22. Mesh-sensitivity test for the aerodynamics of the NREL 5-MW wind turbine.

minimum and maximum thrust and torque, where the difference normalised by the averaged data from the fixed wind turbine simulation is also listed. It is shown that the variance for the thrust is in the range of [-9.56%, +8.36%] while the torque experiences a large variation from −15.11% to +14.23%. It is expected that when the FOWT system works under rough environmental conditions, these time variations of thrust and torque will be certainly more profound, leading to a subsequently variable power output by the wind turbine.

It is also noted that there are a few local minima along the aerodynamic torque curve, which are highlighted as circular markers in Fig. 24 (a), i.e. at the time instants of around 328, 332 and 336 s. These sudden drops of torque, about 5% of the averaged

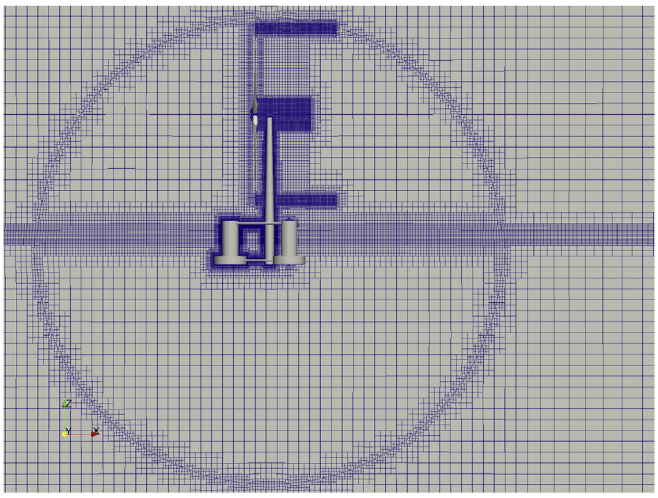

Fig. 23. Mesh of the floating wind turbine.

torque, occur when those three turbine blades pass in front of the tower in sequence, also known as the tower shadow effects. This could be partially reinforced by the time interval of around 4s between two adjacent markers, i.e. one third of the turbine rotation period for a three-bladed turbine. It is therefore clear that Time = 328 s coincides with the instant time when Blade #1 passes in front of the tower, and Time = 332 s and 336 s are for Blades #2 and #3, respectively. The decrease in torque is equivalent to the loss in power as turbine power is defined as torque multiplied by rotational speed. These sudden decreases can also be identified from the aerodynamic thrust curve.

To better understand the tower shadow effects, we analyse the individual torque from a single blade, for example, Blade #1. Fig. 24 (b) shows the aerodynamic torque on Blade #1 with respect to both time and its azimuth angle (α), defined in Fig. 25. Three turbine blades are numbered according to the order in which each blade passes in front of the tower starting from Time = 0 s. Since the turbine rotates clockwise, when viewing from the incoming wind direction, the initial azimuth angle (α) for Blade #1 is 150° while for Blade #2 and #3 it is 30° and 270° respectively. At about Time = 328 s, a dip of the turbine torque is seen from Fig. 24 (a), which is caused by the torque drop of Blade #1 when it is passing in front of the tower as is clearly indicated by its azimuth angle (α) of 180° in Fig. 24 (b). Similarly, for the other two time-instants at Time = 332 s and 336 s, the local descent of the overall turbine torque displayed in Fig. 24(a) are induced by the tower shadow effects when the Blade #2 and #3 are passing across the tower.

Apart from the tower shadow effects, the variation of the aerodynamic torque is directly related to the movement of the floating platform. To better grasp the relationship between wind turbine torque and platform movement, the resultant wind speed component parallel to the wind direction, as defined in Eq. (17), is plotted at three cross sections of Blade #1 in Fig. 24 (b).

Table 6
Mesh-sensitivity test for the aerodynamics of the NREL 5-MW wind turbine (percentage in parentheses shows the difference over data obtained with fine grid).

Grid	Cell Number (in million)	Thrust (kN)	Torque (MN*m)
Coarse	3.83	143.8 (+2.13%)	1.617 (+1.19%)
Medium	5.73	142.0 (+0.85%)	1.602 (+0.25%)
Fine	10.26	140.8 (−)	1.598 (−)

Table 7
Environmental conditions for the FOWT.

Case #	1	2
Wave Amplitude (m)	3.79	
Wave Period (s)	12.1	
Wind Speed (m/s)	7.32	11
Rotor Speed (RPM)	4.95	11.89
Rotor Rotation Period (s)	12.1	5.046

Table 8
Aerodynamic thrust and torque on FOWT under different working conditions (percentage in parentheses shows the difference over averaged data on fixed turbine).

	Thrust (kN)			Torque (MN*m)		
	Case #1	Case #2	Tran [50]	Case #1	Case #2	Tran [50]
Minimum	128.42 (−9.56%)	308.33	632	1.36 (−15.11%)	1.94	3.17
Maximum	153.87 (+8.36%)	398.54	721	1.83 (+14.23%)	2.88	4.25

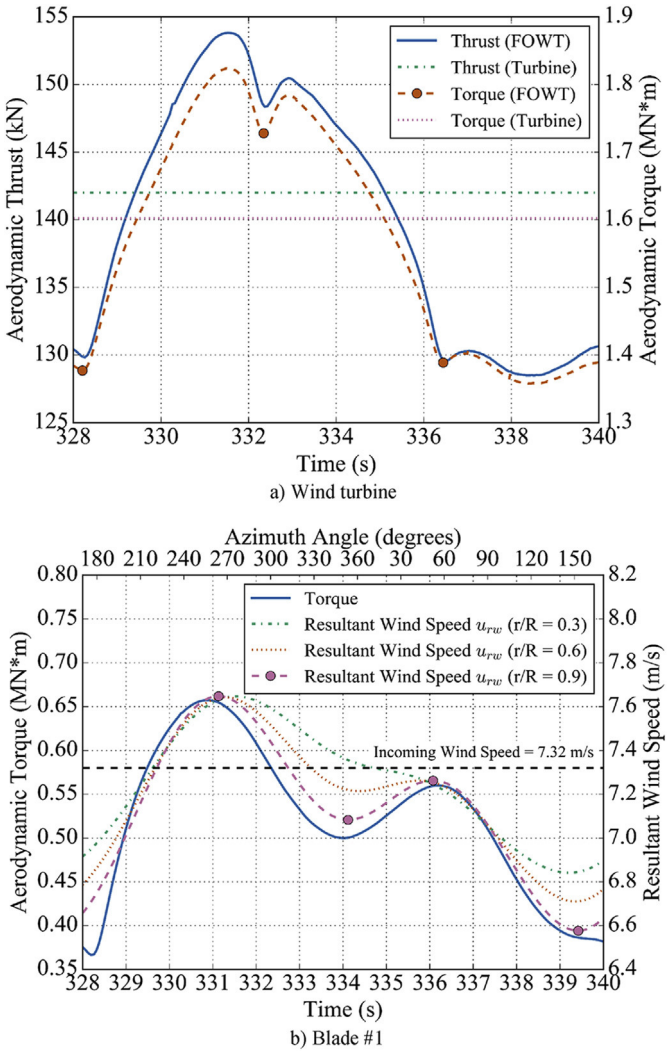

Fig. 24. Aerodynamic thrust and torque on FOWT for Case #1.

$$u_{rw} = u_{wind} - \left[u_{surge} + \omega_{pitch} \cdot (r \cdot \cos\alpha + h + d) \cdot \cos\theta_{pitch}\right] \tag{17}$$

where u_{wind} and u_{surge} are the incoming wind speed and the FOWT system surge velocity separately; θ_{pitch} and ω_{pitch} are the system pitch angle and rotational velocity respectively; α denotes the blade azimuth angle; r represents the distance from the blade cross section to the rotor centre while h and d are the height of the tower and the distance from the system centre of rotation to free surface as shown in Fig. 25.

The cross sections are selected at 30%, 60% and 90% of the blade measuring from the hub centre, i.e. r/R = 0.3, 0.6 and 0.9 in Fig. 24 (b). A strong correlation between the torque on Blade #1 and the resultant wind speed (u_{rw}) at its cross sections can be observed. Taking the curve at r/R = 0.9 as an example, we can see that the torque curve follows the same trend as the resultant speed, i.e. it initially increases with u_{rw} and then decreases. As the resultant wind speed determines the wind speed experienced by the blade undergoing the platform 3DoF motions, it is expected that large thrust and torque occur when the incoming wind speed is high, which partially explains the positive correlation between the time-history of blade torque and the resultant wind speed shown in Fig. 24 (b).

As the aerodynamic toque is the integral representation of pressure on the blade, we plot the pressure coefficient distribution along the blade at three cross sections in Fig. 26, at two typical time instants (i.e. Time = 331 s and 339.5 s), when the blade torque reaches the maximum and minimum respectively in Fig. 24 (b). As expected, at Time = 331 s, the pressure difference between the pressure and suction surfaces is larger than that at Time = 339.5 s, resulting in the maximum torque. This is in accordance with the discussion we presented in the above section.

To discuss the potential variation of turbine performance via different operating conditions such as incoming wind speed and turbine rotational velocity, we extend our above study to Case #2. Fig. 27 presents the aerodynamic thrust and torque for Case #2 at a higher wind speed and turbine rotation speed. As compared to Fig. 24 (a), where the relevant curves are shown for Case #1, the aerodynamic torque varies more in Case #2, indicated by the occurrences of local minima at a regular time interval, due to a higher frequency of the blades passing across the tower in one wave period for Case #2. A comparison is made for the minimum and maximum thrust and torque between Cases #1 and #2 in Table 8. The difference between the two extrema is larger for Case #2 than for Case #1.

To compare the results of the only two CFD studies so far on this FOWT problem, data from Ref. [50] is also listed in Table 8, where the same environmental condition denoted as Case #2 was applied. It can be seen that although the difference between the minima and maxima is very small for two simulations, both our predicted thrust and torque are smaller than the data provided by Ref. [50]. This is likely due to a slightly different wind turbine configuration used in these two studies. Although the same NREL 5-MW baseline turbine geometry is adopted in both studies, the turbine parameters are adjusted. The present study utilises the gross properties from MARIN's model test [8], while Tran and Kim [50] adopted NREL's definition [21]. In particular, the shaft tilt angle and pre-cone angle of the wind turbine are different as are listed in Table 1. In addition, a collective blade pitch angle of 6.4° is applied in this work as was used in MARIN's model test. However, this value is set to zero in the simulations carried out by Tran and Kim [50]. Previous CFD study by Zhao et al. [52] with an identical NREL 5-MW wind turbine geometry using an OpenFOAM solver revealed that increasing the blade pitch angle at high wind speed conditions could significantly decrease the turbine thrust by as much as 50%. Although the present wind speed was not modelled by Zhao et al. [52], the effects of the blade pitch angle on turbine aerodynamic thrust and torque were clearly demonstrated, thus providing the sufficient evidences that the large discrepancy for thrust and torque between the

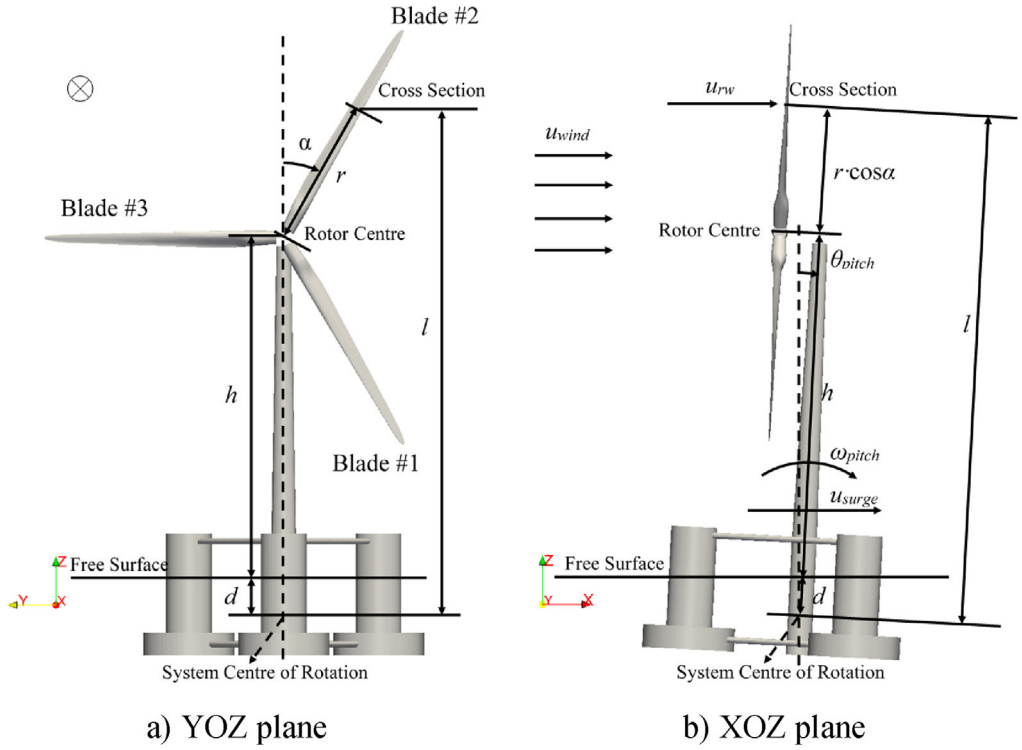

Fig. 25. Definition of azimuth angle and blade numbering (⊗ indicates wind direction).

present study and Tran and Kim [50] could be attributed to the different setting of the above angles. A further study on this issue is undergoing. It is also worth mentioning that the appearance of small thrust and torque can be partially manifested by the model test data in Table 9, where mean thrust from the model tests and the present simulations is summarised with a fixed wind turbine at various environmental conditions. Although the working condition for Case #2 was not experimentally tested, comparison among other similar working conditions indicates the present numerical modelling results are sensible.

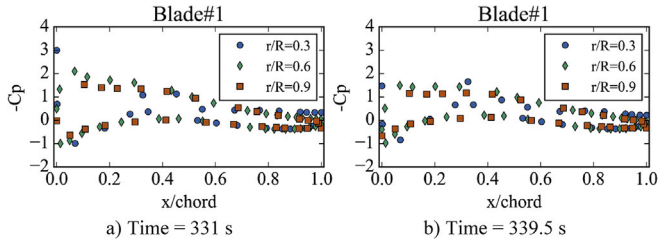

Fig. 26. Pressure coefficient distribution for three cross sections of Blade #1 at different time ('-' represents the negative sign).

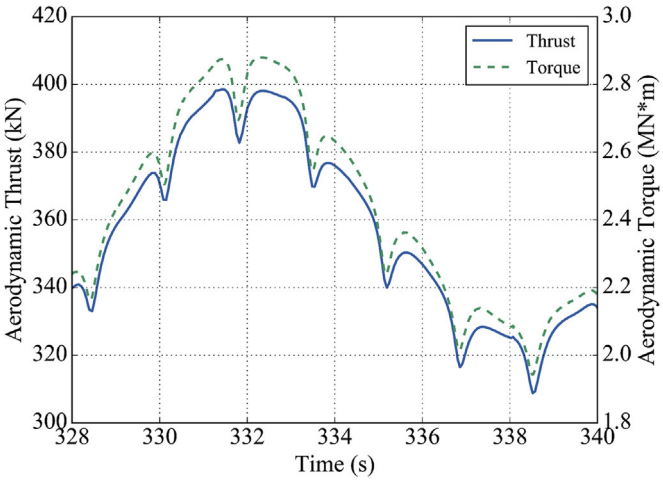

Fig. 27. Aerodynamic thrust and torque on FOWT for Case #2.

Fig. 28 demonstrates the vortex contour of the second invariant of the rate of strain tensor *Q* [25] coloured by velocity component *Ux* for Case #1 within one wave period, where the free surface is also coloured by surface elevation. As can be clearly seen from these figures, strong vortices appear in the vicinity of the blade tips and roots. The presence of the tower also results in a complex flow wake behind the tower. Such detailed flow map and its relation to Fluid-Structure-Interaction (blade and tower) is inevitably useful to identify the potential means for improving wind turbine power output at its design stage, which is currently not possible to achieve using software like FAST.

5.3. Effects of the wind turbine on floating platform hydrodynamic responses

In this Section, the impacts of the wind turbine on the platform

Table 9
Comparison between model test data and present results for a fixed wind turbine under various environmental conditions.

	Mean wind speed (m/s)	Rotor speed (RPM)	Thrust (kN)
Model Test data [8]	7.32	4.95	126.1
	11.23	7.78	202.7
	16.11	9.19	381.7
Present	7.32	4.95	142.0
	11	11.89	353

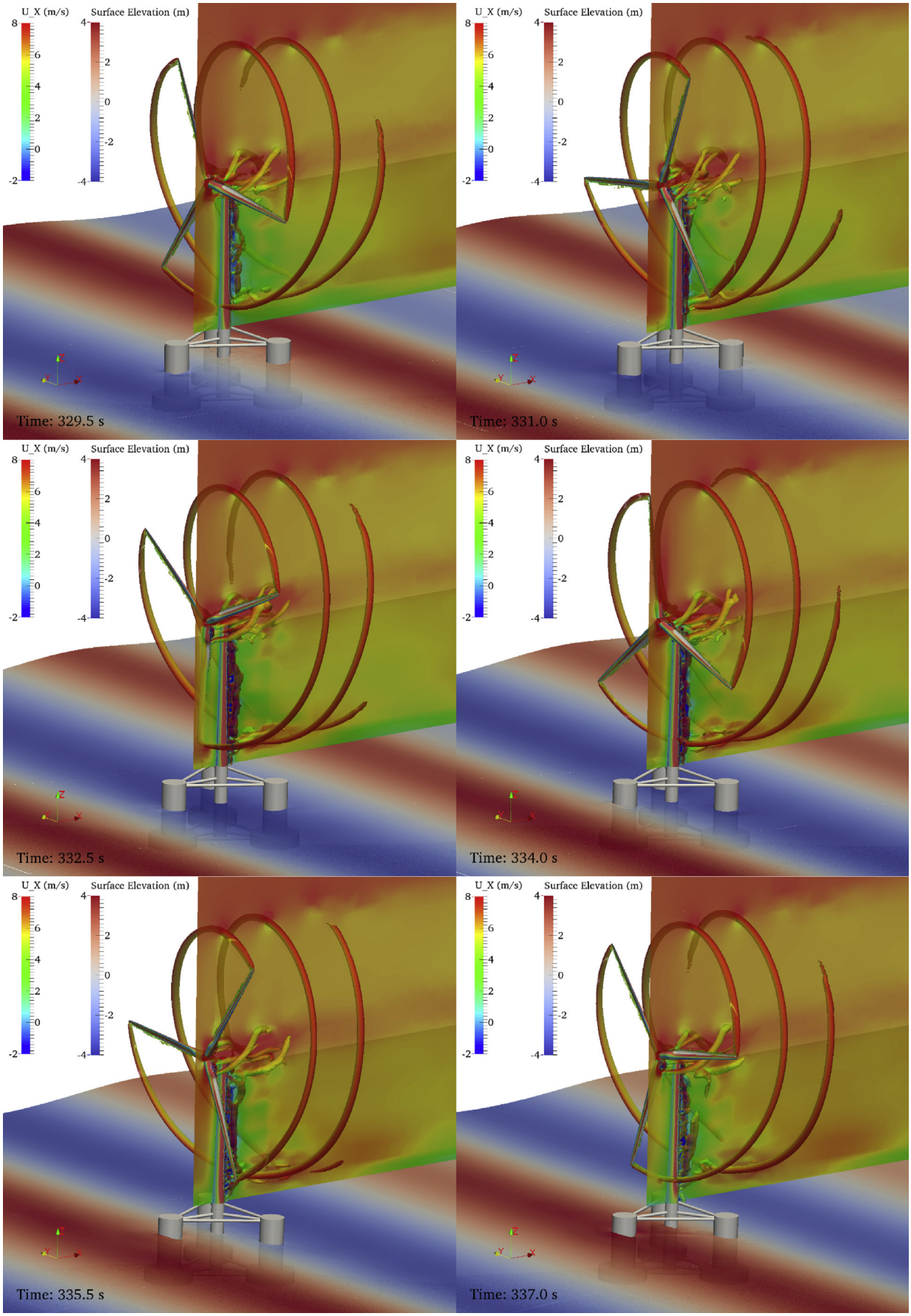

Fig. 28. Vortex contour (Q = 0.25) coloured by velocity component Ux and free surface coloured by surface elevation for Case #1 over one wave period. (For interpretation of the references to colour in this figure legend, the reader is referred to the web version of this article.)

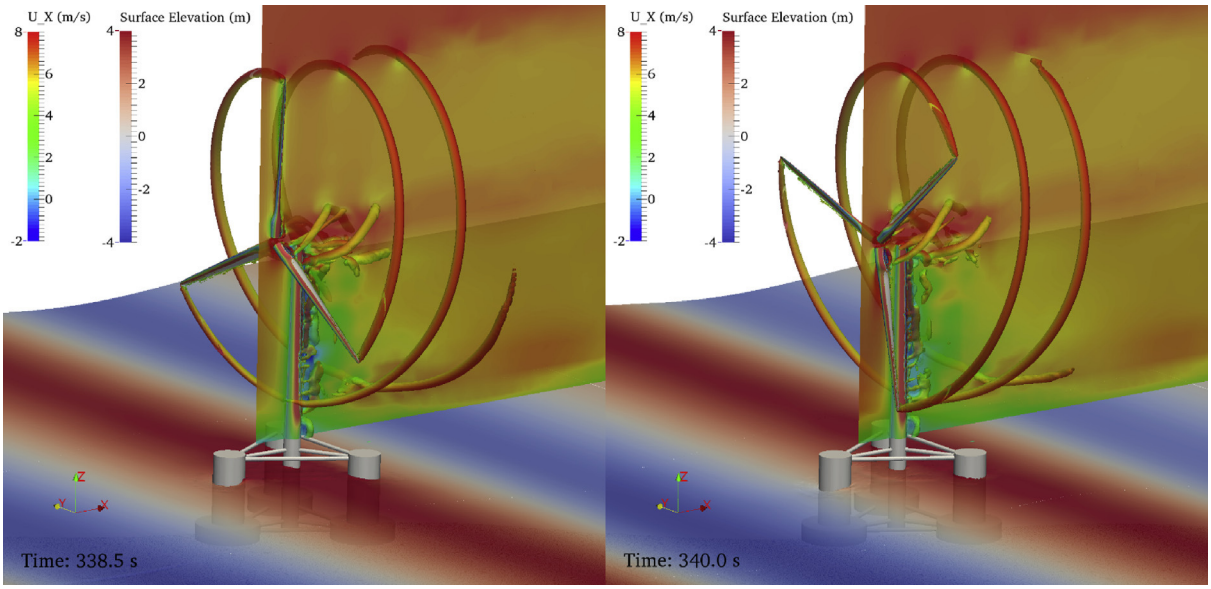

Fig. 28. (*continued*).

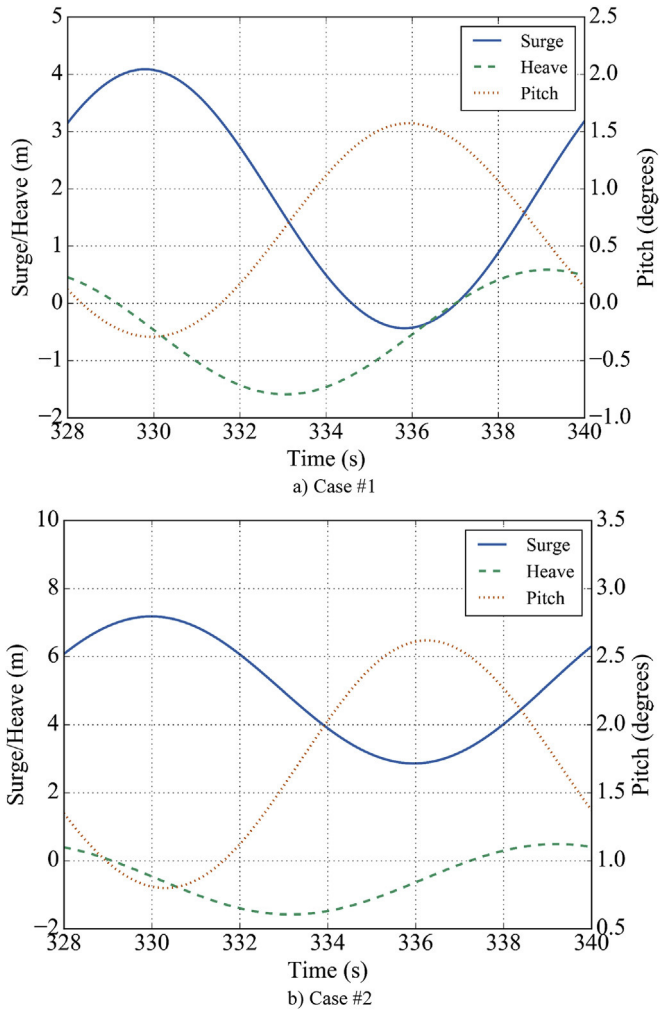

Fig. 29. Time history curves for the motion responses of the floating platform under combined regular waves and steady wind.

are studied by comparing its motion responses under different working conditions, i.e. with/without a wind turbine under operation and with different wind velocity and turbine rotation speed as listed in Table 7.

Time history curves for the surge, heave and pitch motion responses of the floating platform under the combined regular waves and steady wind are plotted in Fig. 29 for both Case #1 and #2. Compared to Fig. 18, where only the floating platform in regular waves is present, some discrepancies can be observed. A comparison is made in terms of the motion RAOs as well as the time-averaged values over the last four wave periods for the three degrees of freedom and listed in Table 10, together with the data from Ref. [50]. It has to be mentioned that because of the unavailability of MARINE test data for the wind and wave conditions simulated herein, the comparison is only made with the work from Ref. [50]. It is easily seen that the RAOs for all three motion responses do not change much in the present study, with a variation of less than 3%, when the turbine operates at a constant rotation speed in a steady wind speed condition. The surge and heave RAOs from Ref. [50] also agree well with our results, with the only exception of the pitch RAO, where the deviation from the no-wind condition is as large as 21%. As is pointed out in Section 5.2, this might be attributed to the different gross properties of the FOWT used in both studies, such as the turbine mass and platform pitch inertia indicated in Table 1. Nevertheless, the very close agreement for the predicted surge and heave RAOs between two different tools demonstrates again the good capability of our CFD tool developed for the study of the hydrodynamics of an FOWT.

Fig. 30 illustrates both the hydrodynamic and aerodynamic loading in the wave propagation direction acting on the floating system for Case #1. Compared to the large variation of the hydrodynamic force at a magnitude order of 10 MN, the aerodynamic force merely changes by about 30 KN as already indicated in Fig. 24 and acts almost like a constant loading, which partially explains why the surge RAO is not affected significantly by the operating wind turbine. The barely noticeable change for the RAO of other two motion responses can be justified in a similar manner.

In contrast to the above motion RAOs, the mean motion responses are remarkably affected by the presence of an operating wind turbine. It is shown from Table 10 that the mean surge

Table 10
Comparison for RAO and mean values of the floating system motion responses under different working conditions (percentage in parentheses shows the difference over data under wave only condition).

	RAO (m/m, m/m, °/m)				Mean value (m, m, °)			
	No wind	Case #1	Case #2	Tran [50]	No wind	Case #1	Case #2	Tran [50]
Surge	0.5965	0.6051 (+1.44%)	0.5947 (−0.30%)	0.5937	0.8686	1.8619	5.0866	9.62
Heave	0.2820	0.2876 (+1.99%)	0.2739 (−2.87%)	0.2850	−0.4538	−0.5030	−0.5391	−0.26
Pitch	0.2470	0.2496 (+1.05%)	0.2424 (−1.86%)	0.2995	0.0156	0.6416	1.7022	3.24

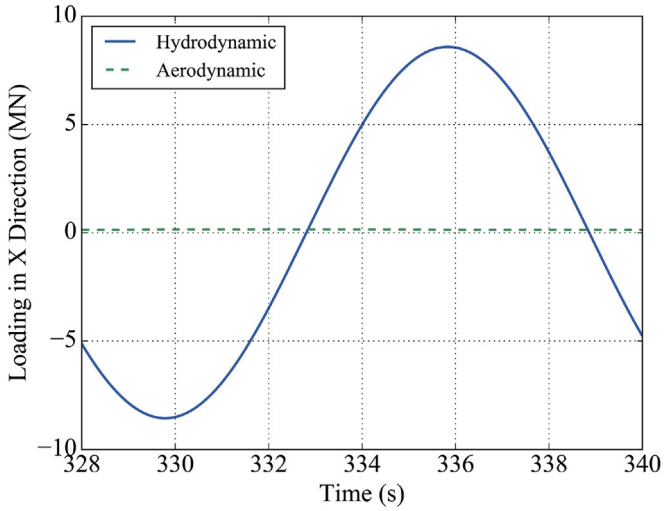

Fig. 30. Comparison between hydrodynamic and aerodynamic loading on the floating system for Case #1.

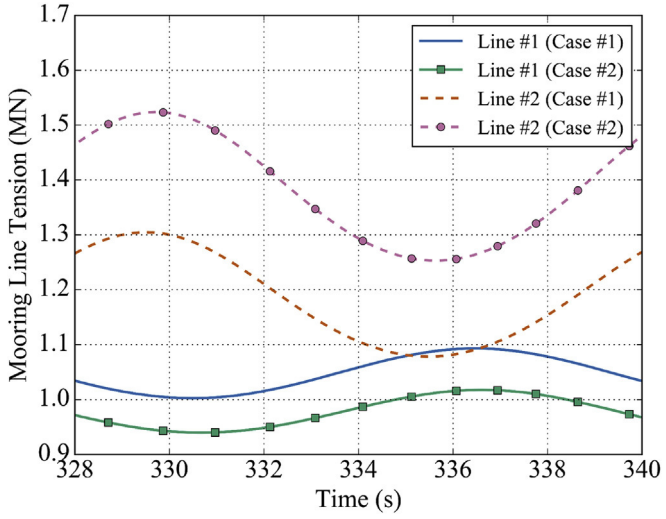

Fig. 31. Mooring line tension for lines #1 and #2 of the floating platform under combined regular waves and steady wind.

increases greatly from 0.8686 m under the wave only condition, to 1.8619 m for Case #1, and further to 5.0866 m for Case #2, where both the wind speed and turbine rotation speed increase. The mean pitch of the platform shifts from near zero to 0.642° for Case #1 and 1.7° for Case #2. Obviously, the aerodynamic thrust induced by the operating turbine, pushes the platform further away in the down-wind direction thus leads to an increase in the mean surge. Meanwhile, the pitching moment resulting from the thrust, due to the large distance from the turbine rotation centre to the system mass centre, which is about 100 m, generates a non-zero pitch angle. Since the aerodynamic thrust for Case #2 is larger than Case #1, the time-averaged surge and pitch are also more significant. An even larger thrust obtained from the work of [50] yields the maximum surge and pitch motions among all the cases shown in Table 10. As to the heave motion, the mean value also changes, although to a relatively less degree than the other two motion responses. The downward movement is possibly attributed to the positive mean pitch angle, which alters the attitude of the floating platform. The mean heave response deviation from that obtained by Ref. [50] is also not to be neglected as it varies from zero to −0.26 m possibly due to the larger mean pitch angle.

In order to illustrate the influence of the wind turbine on the mooring system of the floating platform, the mooring line tension for lines #1 and #2 in both Cases #1 and #2 is plotted in Fig. 31. The RAOs, mean and maximum of the line tensions for mooring line #2 are summarised in Table 11 for all working conditions, as well as the percentage differences over the corresponding data under the wave only condition. Mooring line #2 in the head wave direction is selected for analysis as it consistently experiences larger tension than mooring line #1 in the back wave direction. Due to an increased surge response caused by the additional aerodynamic thrust, the line tension increases when the wind turbine operates in steady wind. For Case #2, the maximum line tension increases by 17.9% and the mean line tension by 16.75% as compared to the case under the wave only condition. It is noted that, in the work of [50], such increments are even more profound. The line tension RAOs also become larger when the aerodynamic thrust is added to the system, which is different from the platform motion RAOs. The increase in the line tension RAOs was also observed in the results provided by Ref. [50]; where this value was about 28.342 kN/m under the wave only condition but rose significantly to 74.142 kN/m under the specified combined wind-wave condition. As pointed out by Hall and Goupee [12], the increase in the mooring line tension RAOs was related to the nonlinear force-displacement relationship of the mooring lines.

6. Conclusions

In this paper, a CFD tool developed to study an offshore floating

Table 11
Comparison for the tension of the line #2 under different working conditions (percentage in parentheses shows the difference over data under wave only condition).

	No wind	Case #1	Case #2	Tran [50]
RAO (kN/m)	27.546	30.324 (+10.08%)	37.509 (+23.69%)	74.142
Mean value (MN)	1.146	1.194 (+4.19%)	1.394 (+16.75%)	2.134
Maximum value (MN)	1.251	1.313 (+4.96%)	1.548 (+17.90%)	2.415

wind turbine system in unsteady viscous flows has been described. The modelling tool is established via an open source framework OpenFOAM with our further developments on a numerical wave tank module and a static mooring line analysis module. With the aid of the sliding mesh technique dealing with multiple cell zones, a fully coupled FOWT system comprising a wind turbine, its floating platform and mooring system was successfully modelled.

A series of simulations was firstly carried out to validate the results with published data and illustrated the accuracy of the tool to predict the above-mentioned three components individually. It was then further applied to the OC4 DeepCWind semi-submersible FOWT. By analysing in detail the motion responses of the floating platform, the vortex induced by the wind turbine and the forces on the blades, we demonstrated the existence of mutual interactions between the wind turbine and its supporting platform, the extent to which depends very much on the environmental conditions, i.e. the wind speed and ocean wave. In particular, the platform responses in surge and pitch impel the turbine to interact with incoming wind, the rotation of turbine and thus the vortices in the downstream of turbine, which further leads to the variation of its aerodynamic thrust and torque.

The influence of the wind turbine on the floating semi-submersible platform was also studied, and the observations are consistent with other simplified models. In particular, the aerodynamic thrust from the wind turbine displaces the platform further in surge motion. Meanwhile, due to the large distance between the turbine rotation centre and the system mass centre, the substantial pitching moment from the turbine thrust force results in a shifted mean pitch motion of the platform. The mooring loading for the mooring line in the head wave direction increases as a result of the large time-averaged surge movement. The dynamic motion responses of the floating system are largely augmented when the rated wind speed and a faster turbine rotation speed are applied.

As a whole, the general results obtained from our CFD tool are in line with other simplified industrial models, such as FAST, under the wind and wave conditions considered herein. However, with the use of the CFD tool we developed, it becomes possible to provide detailed information on the flow field and aerodynamic loading distribution around the wind turbine blades as well as the vortex wake structure in the downstream of turbine, which cannot be obtained from simple models. We believe that a deep understanding on the flow physics would help a better control of FOWT's fluid-structure-interaction, the turbine blades stall and the dynamic motion responses of floating platforms, thus to improve the power efficiency and survivability performance of FOWTs.

At this stage, the model studied herein only considers steady wind, regular wave and rigid wind turbine blades. In our near future studies, more realistic environment conditions will be investigated, which will include large wave amplitudes, irregular wave, unsteady wind and various wind-wave directions, etc. Aeroelasticity of blades is also an important issue for modern large scale offshore wind turbines with long slender blades. It is already noted that the behaviour of deformable blades affects the blades and turbine structural stress and thus the sustainability of renewable energy devices under large unsteady wind conditions. An aeroelastic analysis tool is currently under development by coupling this CFD tool with an open source Multi-Body Dynamics solver to take blade aero-elasticity into consideration. A systematic study for an FOWT with aero-elastic wind turbine blades will be reported in another separate paper.

Acknowledgements

Results were obtained using the EPSRC funded ARCHIE-WeSt High Performance Computer (www.archie-west.ac.uk). EPSRC grant No. EP/K000586/1. This work also used the ARCHER UK National Supercomputing Service (http://www.archer.ac.uk). The first author would like to acknowledge Électricité de France for providing a scholarship for his PhD research. The authors are also grateful to the UK Royal Society and China National Science Foundation Council (NSFC) for partial support of this work. Royal Society grant No. IE131059.

References

[1] R. Antonutti, C. Peyrard, A. Incecik, D. Ingram, L. Johanning, Dynamic Mooring Simulation with Code Aster with Application to a Floating Wind Turbine, 2016 (Manuscript submitted for publication).
[2] S.F. Baudic, A.N. Williams, A. Kareem, A two-dimensional numerical wave Flume—Part 1: nonlinear wave generation, propagation, and absorption, J. Offshore Mech. Arct. Eng. 123 (2) (2001) 70–75.
[3] I. Bayati, J. Jonkman, A. Robertson, A. Platt, The effects of second-order hydrodynamics on a semisubmersible floating offshore wind turbine, J. Phys. Conf. Ser. 524 (1) (2014) 012094.
[4] BBC, Floating Wind Farm to Be Installed off Peterhead, 2015. Available from: http://www.bbc.co.uk/news/uk-scotland-scotland-business-34694463.
[5] M.A. Benitz, D.P. Schmidt, M.A. Lackner, G.M. Stewart, J. Jonkman, A. Robertson, Comparison of hydrodynamic load predictions between reduced order engineering models and computational fluid dynamics for the OC4-DeepCwind semi-submersible, in: Proceedings of the ASME 2014 33rd International Conference on Ocean, Offshore and Arctic Engineering, San Francisco, California, USA, 2014, p. 11.
[6] D. Boger, E. Paterson, R.W. Noack, FoamedOver: a dynamic overset grid implementation in OpenFOAM, in: Proceedings of the 10th Symposium on Overset Composite Grids and Solution Technology, NASA Ames Research Center, Moffet Field, CA, USA, 2010.
[7] H. Cao, D. Wan, Development of multidirectional nonlinear numerical wave tank by naoe-FOAM-SJTU solver, Int. J. Ocean Syst. Eng. 4 (1) (2014) 52–59.
[8] A.J. Coulling, A.J. Goupee, A.N. Robertson, J.M. Jonkman, H.J. Dagher, Validation of a FAST semi-submersible floating wind turbine numerical model with DeepCwind test data, J. Renew. Sustain. Energy 5 (2) (2013) 29.
[9] F. Duan, Z. Hu, J.M. Niedzwecki, Model test investigation of a spar floating wind turbine, Mar. Struct. 49 (2016) 76–96.
[10] EWEA, Aiming High: Rewarding Ambition in Wind Energy, 2015, p. 40.
[11] T. Fan, D. Qiao, J. Ou, Optimized design of equivalent truncated mooring system based on similarity of static and damping characteristics, in: The Twenty-second International Offshore and Polar Engineering Conference, Rhodes, Greece, 2012, pp. 959–966.
[12] M. Hall, A. Goupee, Validation of a lumped-mass mooring line model with DeepCwind semisubmersible model test data, Ocean. Eng. 104 (2015) 590–603.
[13] M.M. Hand, D. Simms, L. Fingersh, D. Jager, J. Cotrell, S. Schreck, S. Larwood, Unsteady Aerodynamics Experiment Phase VI: Wind Tunnel Test Configurations and Available Data Campaigns, 2001.
[14] M.O.L. Hansen, J.N. Sørensen, S. Voutsinas, N. Sørensen, H.A. Madsen, State of the art in wind turbine aerodynamics and aeroelasticity, Prog. Aerosp. Sci. 42 (4) (2006) 285–330.
[15] C.W. Hirt, B.D. Nichols, Volume of fluid (VOF) method for the dynamics of free boundaries, J. Comput. Phys. 39 (1) (1981) 201–225.
[16] M.-C. Hsu, I. Akkerman, Y. Bazilevs, Finite element simulation of wind turbine aerodynamics: validation study using NREL Phase VI experiment, Wind Energy 17 (3) (2014) 461–481.
[17] M. Hsu, Wind Energy Research Webpage, 2015. Available from: http://www.public.iastate.edu/~jmchsu/Research_Wind_Energy.html.
[18] M. Jeon, S. Lee, S. Lee, Unsteady aerodynamics of offshore floating wind turbines in platform pitching motion using vortex lattice method, Renew. Energy 65 (2014) 207–212.
[19] J.M. Jonkman, Dynamics Modeling and Loads Analysis of an Offshore Floating Wind Turbine, Doctoral Dissertation, University of Colorado at Boulder, Boulder, Colorado, 2007.
[20] J.M. Jonkman, Dynamics of offshore floating wind turbines—model development and verification, Wind Energy 12 (5) (2009) 459–492.
[21] J.M. Jonkman, S. Butterfield, W. Musial, G. Scott, Definition of a 5-MW Reference Wind Turbine for Offshore System Development, 2009, p. 63.
[22] B.J. Koo, A.J. Goupee, R.W. Kimball, K.F. Lambrakos, Model tests for a floating wind turbine on three different floaters, J. Offshore Mech. Arct. Eng. 136 (2) (2014) 020907.
[23] J. Larsen, H. Dancy, Open boundaries in short wave simulations—a new approach, Coast. Eng. 7 (3) (1983) 285–297.
[24] P. Li, P. Cheng, D. Wan, Q. Xiao, Numerical simulations of wake flows of floating offshore wind turbines by unsteady actuator line model, in: The 9th International Workshop on Ship and Marine Hydrodynamics, Glasgow, UK, 2015.
[25] Y. Li, K.-J. Paik, T. Xing, P.M. Carrica, Dynamic overset CFD simulations of wind turbine aerodynamics, Renew. Energy 37 (1) (2012) 285–298.

[26] Y. Liu, Y. Peng, D. Wan, Numerical investigation on interaction between a semi-submersible platform and its mooring system, in: ASME 2015 34th International Conference on Ocean, Offshore and Arctic Engineering, St. John's, Newfoundland, Canada, 2015. V007T06A071–V007T06A071.
[27] Y. Liu, Q. Xiao, A. Incecik, D.-C. Wan, Investigation of the effects of platform motion on the aerodynamics of a floating offshore wind turbine, J. Hydrodynamics, Ser. B 28 (1) (2016) 95–101.
[28] M. Masciola, A. Robertson, J. Jonkman, A. Coulling, A. Goupee, Assessment of the importance of mooring dynamics on the global response of the DeepC-wind floating semisubmersible offshore wind turbine, in: Proceedings of the Twenty-third (2013) International Offshore and Polar Engineering, Anchorage, Alaska, USA, 2013, pp. 359–368.
[29] F.R. Menter, Review of the shear-stress transport turbulence model experience from an industrial perspective, Int. J. Comput. Fluid Dyn. 23 (4) (2009) 305–316.
[30] A. Nematbakhsh, E.E. Bachynski, Z. Gao, T. Moan, Comparison of wave load effects on a TLP wind turbine by using computational fluid dynamics and potential flow theory approaches, Appl. Ocean Res. 53 (2015) 142–154.
[31] A. Nematbakhsh, D.J. Olinger, G. Tryggvason, Nonlinear simulation of a spar buoy floating wind turbine under extreme ocean conditions, J. Renew. Sustain. Energy 6 (3) (2014) 20.
[32] OpenFOAM, Arbitrary Mesh Interface (AMI), 2011. Available from: http://www.openfoam.org/version2.1.0/ami.php.
[33] OpenFOAM, Mesh Generation with the SnappyHexMesh Utility, 2013. Available from: http://www.openfoam.org/docs/user/snappyHexMesh.php#x26-1510005.4.
[34] OpenFOAM, The OpenFOAM Website, 2015. Available from: http://www.openfoam.com/.
[35] S. Quallen, T. Xing, P. Carrica, Y. Li, J. Xu, CFD simulation of a floating offshore wind turbine system using a quasi-static crowfoot mooring-line model, J. Ocean Wind Energy 1 (3) (2014) 143–152.
[36] N. Ren, Y. Li, J. Ou, Coupled wind-wave time domain analysis of floating offshore wind turbine based on Computational Fluid Dynamics method, J. Renew. Sustain. Energy 6 (2) (2014), 023106–1-13.
[37] A. Robertson, J. Jonkman, M. Masciola, H. Song, A. Goupee, A. Coulling, C. Luan, Definition of the Semisubmersible Floating System for Phase II of OC4, 2014.
[38] A. Robertson, J. Jonkman, F. Vorpahl, W. Popko, J. Qvist, L. Frøyd, X. Chen, J. Azcona, E. Uzunoglu, C.G. Soares, Offshore code comparison collaboration continuation within IEA Wind Task 30: phase II results regarding a floating semisubmersible wind system, in: ASME 2014 33rd International Conference on Ocean, Offshore and Arctic Engineering, San Francisco, California, 2014b. V09BT09A012–V09BT09A012.
[39] H. Rusche, Computational Fluid Dynamics of Dispersed Two-phase Flows at High Phase Fractions, Doctoral Dissertation, University of London, London, 2002.
[40] T. Sebastian, M.A. Lackner, Development of a free vortex wake method code for offshore floating wind turbines, Renew. Energy 46 (2012) 269–275.
[41] Z.-R. Shen, D.-C. Wan, An irregular wave generating approach based on naoe-FOAM-SJTU solver, China Ocean. Eng. 30 (2) (2016) 177–192.
[42] Z. Shen, H. Cao, H. Ye, Y. Liu, D. Wan, in: Development of CFD Solver for Ship and Ocean Engineering Flows. 8th International OpenFOAM Workshop, Jeju, Korea, 2013.
[43] Z. Shen, D. Wan, RANS computations of added resistance and motions of a ship in head waves, Int. J. Offshore Polar Eng. 23 (4) (2013) 263–271.
[44] Z. Shen, D. Wan, P.M. Carrica, Dynamic overset grids in OpenFOAM with application to KCS self-propulsion and maneuvering, Ocean. Eng. 108 (2015) 287–306.
[45] H. Shin, S. Cho, K. Jung, Model test of an inverted conical cylinder floating offshore wind turbine moored by a spring-tensioned-leg, Int. J. Nav. Archit. Ocean Eng. 6 (1) (2014) 1–13.
[46] B. Skaare, T. Hanson, R. Yttervik, F. Nielsen, Dynamic response and control of the hywind demo floating wind turbine, in: European Wind Energy Conference, Warsaw, Poland, 2011.
[47] T. Tran, D. Kim, J. Song, Computational fluid dynamic analysis of a floating offshore wind turbine experiencing platform pitching motion, Energies 7 (8) (2014) 5011–5026.
[48] T.T. Tran, D.-H. Kim, The coupled dynamic response computation for a semi-submersible platform of floating offshore wind turbine, J. Wind Eng. Industrial Aerodynamics 147 (2015) 104–119.
[49] T.T. Tran, D.-H. Kim, A CFD study into the influence of unsteady aerodynamic interference on wind turbine surge motion, Renew. Energy 90 (2016a) 204–228.
[50] T.T. Tran, D.-H. Kim, Fully coupled aero-hydrodynamic analysis of a semi-submersible FOWT using a dynamic fluid body interaction approach, Renew. Energy 92 (2016b) 244–261.
[51] T. Utsunomiya, H. Matsukuma, S. Minoura, K. Ko, H. Hamamura, O. Kobayashi, I. Sato, Y. Nomoto, K. Yasui, At sea experiment of a hybrid spar for floating offshore wind turbine using 1/10-scale model, J. Offshore Mech. Arct. Eng. 135 (3) (2013), 034503–1-8.
[52] W. Zhao, P. Cheng, D. Wan, in: Numerical Computation of Aerodynamic Performances of NREL Offshore 5-MW Baseline Wind Turbine. The Eleventh ISOPE Pacific/Asia Offshore Mechanics Symposium, Shanghai, China, 2014, pp. 13–18.
[53] W. Zhao, D. Wan, Numerical study of interactions between phase II of OC4 wind turbine and its semi-submersible floating support system, J. Ocean Wind Energy 2 (1) (2015) 45–53.